

AD A044073



12

PSI TR-91

**THEORETICAL STUDY OF LASER-INDUCED
BREAKDOWN IN PARTICLE-CONTAMINATED AIR**

by

R. G. Root, P. K. S. Wu and A. N. Pirri

May 1977

Final Report for Period 15 September 1976 — 15 March 1977

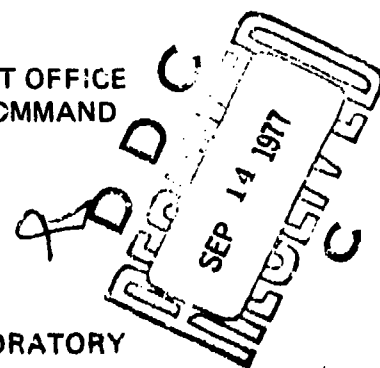
Approved for Public Release; Distribution Unlimited

Prepared for

HIGH ENERGY LASER PROJECT OFFICE
U. S. NAVAL SEA SYSTEMS COMMAND
Washington, D.C.

Monitored by

U. S. NAVAL RESEARCH LABORATORY
Washington, D.C.



Contract No. N00173-76-C-0329

PHYSICAL SCIENCES INC.
30 COMMERCE WAY, WOBURN, MASS. 01801

(7) Final rept. 15 Sep 71 - 15 Mar 77

UNCLASSIFIED

SECURITY CLASSIFICATION OF THIS PAGE (When Data Entered)

REPORT DOCUMENTATION PAGE		READ INSTRUCTIONS BEFORE COMPLETING FORM
1. REPORT NUMBER	2. GOVT ACCESSION NO.	3. RECIPIENT'S CATALOG NUMBER
4. TITLE (and Subtitle) Theoretical Study of Laser-Induced Breakdown in Particle-Contaminated Air		5. TYPE OF REPORT & PERIOD COVERED FINAL REPORT 9/15/76-3/15/77
7. AUTHOR(s) R.G./Root, P.K.S./Wu A. N./Pirri		6. PERFORMING ORG. REPORT NUMBER PSI-TR-91
9. PERFORMING ORGANIZATION NAME AND ADDRESS Physical Sciences Inc. 30 Commerce Way Woburn, MA 01801		14. CONTRACT OR GRANT NUMBER(s) N00173-76-C-0329
11. CONTROLLING OFFICE NAME AND ADDRESS High Energy Laser Project Office U. S. Naval Sea Systems Command Washington, D. C.		10. PROGRAM ELEMENT, PROJECT, TASK AREA & WORK UNIT NUMBERS
13. MONITORING AGENCY NAME & ADDRESS (if different from Controlling Office) U. S. Naval Research Laboratory Washington, D. C.		12. REPORT DATE May 77
		13. NUMBER OF PAGES 96
		15. SECURITY CLASS (of this report) Unclassified
		15a. DECLASSIFICATION/DOWNGRADING SCHEDULE
16. DISTRIBUTION STATEMENT (of this Report) Approved for Public Release; Distribution Unlimited		
17. DISTRIBUTION STATEMENT (of the abstract entered in Block 20, if different from Report)		
18. SUPPLEMENTARY NOTES		
19. KEY WORDS (Continue on reverse side if necessary and identify by block number) Laser effects Vapor Heating Air Breakdown Plasma Growth Particulates, Al ₂ O ₃		
20. ABSTRACT (Continue on reverse side if necessary and identify by block number) Of the physical effects that limit the propagation of a high intensity laser beam through the atmosphere, air breakdown has the most catastrophic influence. Completely ionized air attenuates 10.6 μ radiation within a few centimeters. It is therefore imperative that the threshold for air breakdown under realistic circumstances be determined. In this report the physics of long pulse laser-induced breakdown process in particle-		

DD FORM 1473 1 JAN 73

EDITION OF 1 NOV 68 IS OBSOLETE

UNCLASSIFIED 391105
SECURITY CLASSIFICATION OF THIS PAGE (When Data Entered)

SECURITY CLASSIFICATION OF THIS PAGE: When Data Entered

Accession for
NYS
DOC
Transcript
History
BY
DISPATCHED
To
A

SECURITY CLASSIFICATION OF THIS PAGE(When Data Entered)

PSI TR-91

**THEORETICAL STUDY OF LASER-INDUCED
BREAKDOWN IN PARTICLE-CONTAMINATED AIR**

R. G. Root, P. K.S. Wu and A. N. Pirri

**PHYSICAL SCIENCES INC.
30 Commerce Way
Woburn, MA 01801**

May 1977

Final Report for Period 15 September 1976 - 15 March 1977

Approved for Public Release; Distribution Unlimited

Prepared for

**HIGH ENERGY LASER PROJECT OFFICE
U. S. NAVAL SEA SYSTEMS COMMAND
Washington, D. C.**

Monitored by

**U. S. NAVAL RESEARCH LABORATORY
Washington, D. C.**

Contract No. N00173-76-C-0329

ACKNOWLEDGEMENT

This research was performed under Contract N00173-76-C-0329 during the period September 1976 - April 1977. It was monitored by Dr. P. B. Ulrich of the U. S. Naval Research Laboratory with funds provided by the High Energy Laser Project Office (PMS-405) of the U. S. Naval Sea Systems Command.

ABSTRACT

Of the physical effects that limit the propagation of a high intensity laser beam through the atmosphere, air breakdown has the most catastrophic influence. Completely ionized air attenuates 10.6μ radiation within a few centimeters. It is therefore imperative that the threshold for air breakdown under realistic circumstances be determined. In this report the physics of long pulse laser-induced breakdown process in particle-contaminated air is studied in four stages. The first stage is particulate heating and vaporization. Simple models are used to predict the time to vaporization at the particle surface, the time to vaporize a given fraction of the particle, and the pressure of the vapor immediately above the particle surface. The second stage is the heating of the vapor cloud. The heating rate is calculated under two approximations. For a short time period after the vapor cloud is formed, its central region is assumed to be effectively insulated from the air, and thermal conduction losses can be neglected. At later times thermal conduction losses are important throughout the whole cloud; then a model in which the conduction losses are averaged over the volume of the vapor is used. Using these models we are able to estimate the time for the vapor cloud to reach a high temperature (nominally chosen to be $20,000^{\circ}\text{K}$) and the minimum laser intensity required to heat the vapor cloud. The third stage of the breakdown process is the creation of air plasma. An estimate is made of the temperature the surrounding air must reach in order to readily absorb the laser energy. Then, from crude estimates of the energy flux into the air, the rate of expansion of the plasma into the air is determined. The final stage is the growth of the air plasma. The growth is followed as a function of time for various values of the initial air plasma size and the laser intensity.

TABLE OF CONTENTS

	<u>Page</u>
ABSTRACT	iii
1. INTRODUCTION	1
2. PARTICULATE HEATING AND VAPORIZATION	7
3. VAPOR CLOUD HEATING	29
4. CREATION OF AN AIR PLASMA	63
5. AIR PLASMA DYNAMICS	69
6. SUMMARY	87
REFERENCES	89

1. INTRODUCTION

Of the physical effects that limit the propagation of a high intensity laser beam through the atmosphere, air breakdown has the most catastrophic influence. Completely ionized air attenuates 10.6μ radiation within a few centimeters. It is therefore imperative that the threshold for air breakdown under realistic circumstances be determined.

Studies of the breakdown threshold in clean air and the noble gases are numerous, and observed thresholds are in good agreement with an extension of microwave breakdown theory to optical frequencies. When air is contaminated with particles, it has been observed that the breakdown threshold is lowered substantially below the clean air value. The mechanisms by which particles induce breakdown are not clearly understood. However, it is generally accepted that breakdown occurs as a result of vaporization of the particles, heating of the vapor and surrounding air, and ultimately ionization and "breakdown" of the air within the laser beam volume. The sequence of events and the detailed physical processes that occur is strongly dependent upon laser intensity, wavelength and pulse time.

At $10.6\mu\text{m}$ and for short laser pulses ($< 1\mu\text{sec}$) the observed breakdown threshold is one to two orders of magnitude lower than the clean air value for particle sizes from $3\mu\text{m}$ to approximately $30\mu\text{m}$ in diameter.¹ The threshold is fairly insensitive to the particle materials that have been studied and decreases with increasing particle diameter. In addition, for a pulse length of approximately 100 nsec , Lencioni² has found that the breakdown threshold in the presence of particles scales as the inverse square of the laser wavelength. This is consistent with cascade breakdown in either the particle vapor or the air surrounding the particle. Triplett and Boni³ have performed a theoretical study of the interaction of laser radiation with a single suspended particle.

Their analysis applies only when the laser intensity is sufficiently large that the rapidly evaporating or "exploding" particle drives a strong shock wave into the surrounding air. Breakdown then occurs via a nonequilibrium cascade process in either the vapor or shock heated air. Calculations indicate that reductions in the breakdown threshold of slightly greater than one order of magnitude below that of clean air are feasible by this mechanism.

An experimental study of laser-induced breakdown in contaminated air with long (100 μ sec) 10.6 μ m laser pulses was performed by Schlier, Pirri and Reilly.⁴ The most significant result of this study was that the laser intensity for breakdown in contaminated air was almost three orders of magnitude below the clean air value. This result is one to two orders of magnitude below experimental and theoretical predictions for breakdown with microsecond or submicrosecond pulses. In addition, an "incubation" time or delay time between laser turn on and breakdown (as detected by a reduction in the transmitted laser power) was observed. Luminous plasmas were observed during the incubation period. Often a plasma was seen but no breakdown occurred. There is at present no theoretical understanding of the contaminated air breakdown mechanisms for these long laser pulses ($> 10\mu$ sec). Since the observed delay times are 10 - 30 μ sec, the breakdown mechanism cannot be nonequilibrium cascade ionization of shock heated air or vapor. It appears that the vapor formed by the evaporating particle heats in local thermodynamic equilibrium and transfers its energy to the surrounding air by conduction and radiative transport. The air ultimately heats via inverse Bremsstrahlung absorption until the formed plasma becomes opaque to the laser radiation. This plasma formation mechanism is similar to that which leads to the ignition of laser-supported combustion waves above surfaces.^{5,6} The wavelength dependence of long pulse thresholds is unknown at present.

In this report the physics of long pulse laser-induced breakdown process in particle - contaminated air is studied in four stages. The first stage, which is discussed in Section 2, is particulate heating and vaporization. Simple

models are used to predict the time to vaporization at the particle surface, the time to vaporize a given fraction of the particle, and the pressure of the vapor immediately above the particle surface. The second stage, the heating of the vapor cloud, is analyzed in Section 3. The heating rate is calculated under two approximations. For a short time period after the vapor cloud is formed, its central region is assumed to be effectively insulated from the air, and thermal conduction losses can be neglected. At later times thermal conduction losses are important throughout the whole cloud; then a model in which the conduction losses are averaged over the volume of the vapor is used. Using these models we are able to estimate the time for the vapor cloud to reach a high temperature (nominally chosen to be $20,000^{\circ}\text{K}$) and the minimum laser intensity required to heat the vapor cloud. The third stage of the breakdown process, the creation of air plasma, is studied in Section 4. An estimate is made of the temperature the surrounding air must reach in order to readily absorb the laser energy. Then, from crude estimates of the energy flux into the air, the rate of expansion of the plasma into the air is determined. The final stage, the growth of the air plasma, is analyzed in Section 5. The growth is followed as a function of time for various values of the initial air plasma size and the laser intensity.

A plot of the experimentally determined threshold intensity versus time to breakdown is shown in Fig. 1.1 for 10.6μ radiation.¹ The region of interest in this report is the intensity range from $3 \times 10^6 \text{ W/cm}^2$ to $8 \times 10^6 \text{ W/cm}^2$. Spherical particles of Al_2O_3 having a diameter of $30\mu\text{m}$ are observed to cause breakdown within 20 to $100\mu\text{sec}$ from the beginning of the pulse. Glass fibers also lead to similar breakdown times, but they are not analyzed in this report. For comparison with data, numerical calculations are made in each section for Al_2O_3 particles $30\mu\text{m}$ in diameter exposed to 10.6μ radiation of intensity between $3 \times 10^6 \text{ W/cm}^2$ to $8 \times 10^6 \text{ W/cm}^2$.

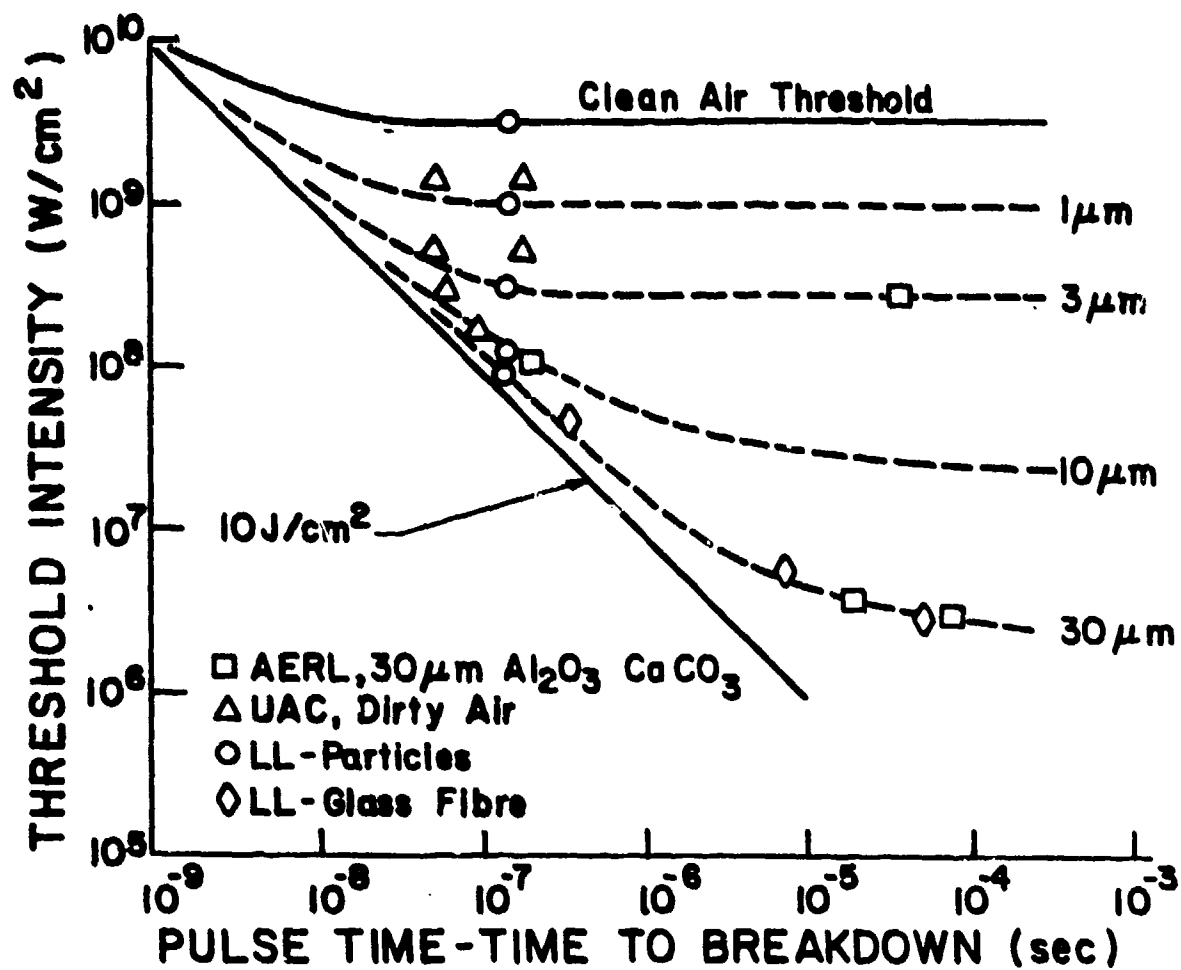


Fig. 1.1 Measurements of Air Breakdown in the Presence of Particulate Matter (From Ref. 1)

Due to the complicated coupling between heating, vapor and air dynamics simple scaling laws for the variation of breakdown time and threshold as a function of laser wavelength and particulate composition can not be given. However, in each stage, the important parameters of the breakdown process which change with wavelength and particulate composition are identified.

In Section 6, this report is concluded with the calculation of the entire breakdown sequence for a laser intensity at $5 \times 10^6 \text{ W/cm}^2$. The conclusions of each of the four stages are summarized and experiments are suggested.

2. PARTICULATE HEATING AND VAPORIZATION

A particulate exposed to a laser beam absorbs energy and thereby increases its temperature. If the beam is intense enough the particle may reach the vaporization temperature. Many interesting phenomena can occur during the process; for example, the particle may move due to the pressure of the vapor, or the particle may shatter because of unequal heating. However, for the purpose of estimating breakdown thresholds the important quantities are the size and composition of the vapor cloud formed by the particle. In this section, therefore, simple models are employed to characterize (1) the time when bulk vaporization begins, (2) the time required to vaporize an arbitrary fraction of the particle, and (3) the pressure of the vapor above the particle surface.

The optical properties of the particulate are determined by its index of refraction which has both a real part n_1 and an imaginary part n_2 ; and by the ratio of the radiation wavelength λ to the radius R of the particulate. For $R \ll \lambda$ the Rayleigh limit for the absorption cross section is approached. For large particles, $R \gg \lambda$, geometric optics applies. If, in addition, the complex index of refraction n obeys $|n - 1| \ll 1$ and $4\pi n_2/R\lambda < 1$, the cross section is given by volume absorption with the bulk absorption coefficient α defined by

$$\alpha = 4\pi n_2/\lambda \quad (2.1)$$

Alternatively, if $4\pi n_2 R/\lambda \gg 1$ the particle acts as a surface absorber. Whenever none of the above mentioned limiting cases applies, Mie theory⁷ should be used.

The optical constants for Al_2O_3 are required input for any determination of the amount of laser energy absorbed. Unfortunately n_1 and n_2 vary rapidly with temperature, wavelength and method of experimental determination. The values reported by several authors^{8,9,10} are listed in Table 2.1. Clearly the experiments based upon particulates differ from the results obtained from bulk samples. According to Toon and Pollack,⁸ experiments using particulates are difficult to interpret correctly. We therefore base our estimates upon the bulk sample experiments. The values for n_2 from Ref. 10 are shown in Fig. 2.1 for various temperatures and wavelengths. The imaginary point of the index of refraction is seen to increase rapidly with wavelength near $10.6\mu\text{m}$ for Al_2O_3 at room temperature. At higher temperature, however, the increase with wavelength is less significant. In breakdown studies the particle is heated from room temperature to the vaporization temperature of 4000°K . Clearly reliable values of the index of refraction over the full temperature range from 300°K to 4000°K are a prerequisite for accurate predictions. In their absence, the values of $n_1 = .8$ and $n_2 = .2$, which were reported in Ref. 10 at $T = 1773^\circ\text{K}$, have been used to characterize the entire heating process. This choice is logical because most of the energy needed to vaporize the particulate must be supplied at the boiling temperature; therefore, the high temperature values of n_2 are most important.

For $n_2 = .2$ and a radius of 15μ , the product of absorption coefficient and R for 10.6μ radiation is 3.6. Mie theory should normally be used in order to describe this regime. Unfortunately the standard Mie theory code¹¹ has not been tested for $n_1 < 1$, and results predicted by it are not guaranteed reliable. Furthermore the code provides information on the scattering rather than the local deposition within the particulate.¹² Instead of modifying the code extensively to overcome these shortcomings, we resorted to ray optics to predict local energy deposition.¹³ The Mie code was used to estimate total absorption and to lend credence to the ray theory prediction.

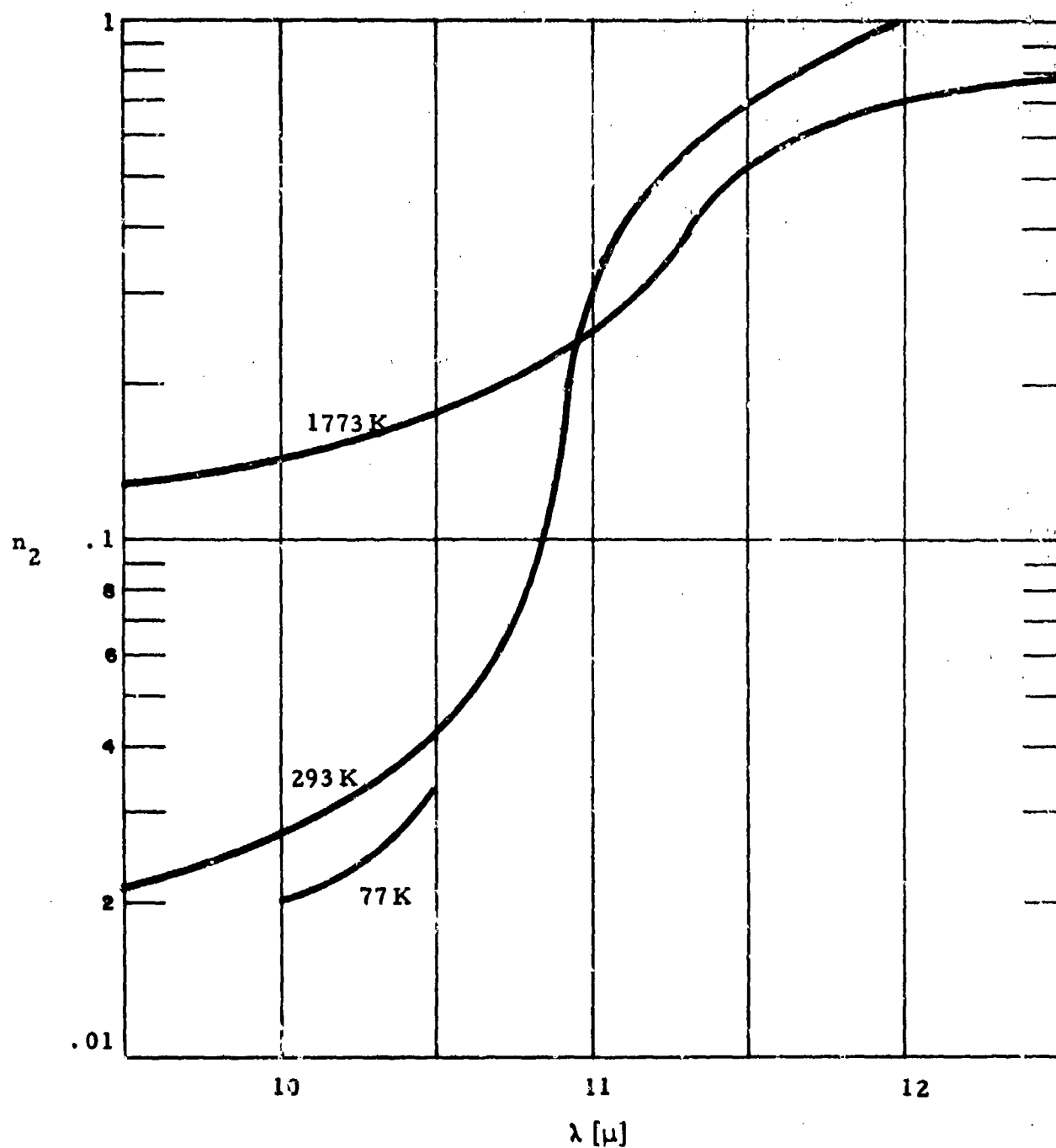


Fig. 2.1 Imaginary Part of the Index of Refraction of Al_2O_3 as a Function of Wavelength for Various Temperatures.

TABLE 2.1

Experimental Values of the Index of Refraction of Al_2O_3

Temperature	$\lambda = 10\mu$ n_1 n_2	$\lambda = 10.6\mu$ n_1 n_2	$\lambda = 11\mu$ n_1 n_2	Ref.	Sample
293 K	.92 .018		.30 .089	8	Bulk
293 K		.488 .048		10	Bulk
300 K	1.15 3.83		.31 .0106	9	Particulate
1773 K		.857 .19		10	Bulk
2000 K	.978 1.31		.713 .34	9	Particulate

In ray optics the path of the radiation through the particulate is determined by the real part of the index of refraction and by Snell's law,

$$n_1 \sin \theta = \sin \theta_A \quad (2.2)$$

where θ_A is the angle between the ray in the air and the normal to the surface, θ is the angle between the ray in the particle and the normal to the surface, and the index of refraction of air has been set to one. Typical rays for $n_1 > 1$ and $n_1 < 1$ are shown in Fig. 2.2a and 2.2b respectively.

The absorption of the radiation is characterized by the bulk attenuation coefficient $\alpha = 4\pi n_2/\lambda$. The local rate of deposition is $\frac{dI}{dz} = \alpha I$ where I is the local radiation flux. In terms of the distance z along the ray from the particulate surface and the incident laser flux, denoted by I_0 , the local deposition attributable to a given ray is $\alpha I_0 e^{-\alpha z}$. Therefore the total absorption of the particle can be written as

$$2\pi \int_0^{y_{\max}} y \, dy \int_0^{2R \cos \theta} dz \, \alpha e^{-\alpha z} I_0$$

where y is the displacement of the incident ray from the ray passing through the center of the particle as shown in Fig. 2.2. Application of Snell's law yields

$$R \cos \theta = R \sqrt{1 - \frac{\sin^2 \theta_A}{n_1^2}} = \sqrt{R^2 - y^2/n_1^2}.$$

The maximum value of y in the integration is R if $n_1 > 1$ and $R n_1$ if $n_1 < 1$.

The total energy absorbed by the particulate can then be expressed as $I_0 \pi R^2 F$, where the efficiency factor F is defined as¹⁴

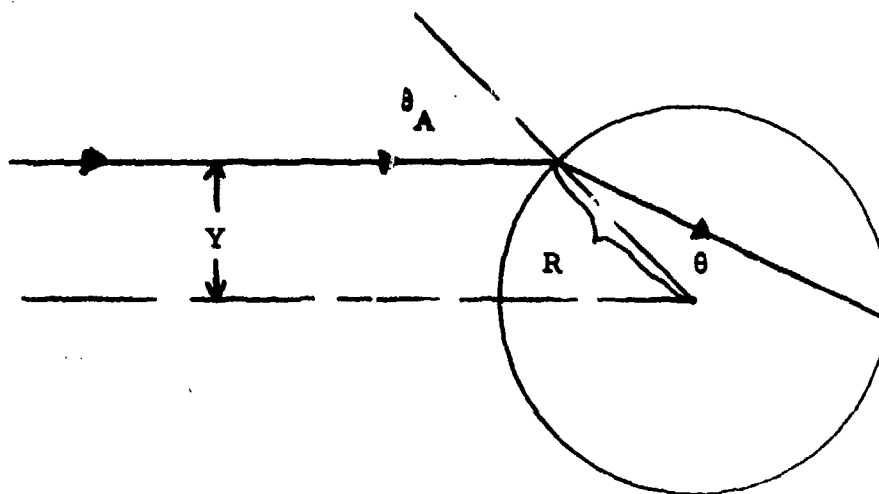


Fig. 2.2a Path of Ray for $n_1 > 1$

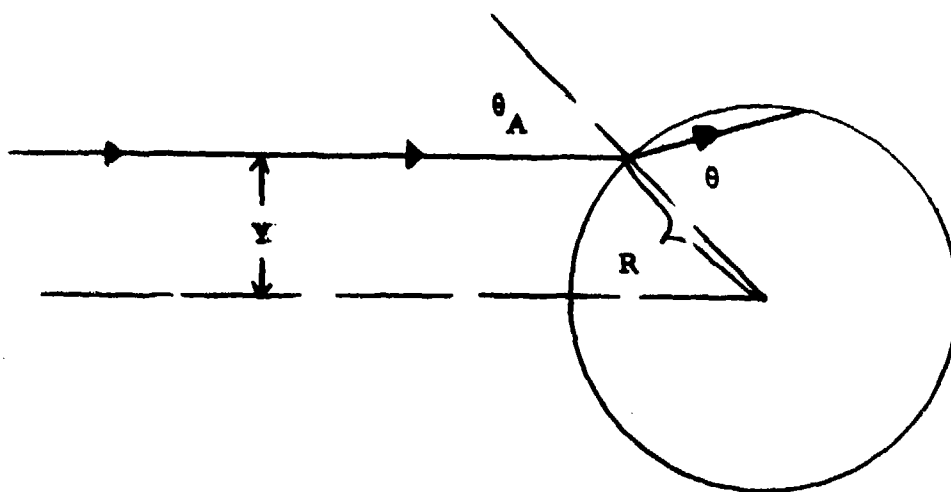


Fig. 2.2b Path of Ray for $n_1 < 1$

$$F = \left(\frac{y_{\max}}{R} \right)^2 - \frac{n_1^2}{2(\alpha R)^2} \left\{ \left[1 + 2\alpha \sqrt{R^2 - \left(\frac{y_{\max}}{n_1} \right)^2} \right] e^{-2\alpha \sqrt{R^2 - \left(\frac{y_{\max}}{n_1} \right)^2}} - (1 + 2\alpha R) e^{-2\alpha R} \right\} \quad (2.3)$$

Results obtained by using Eq. (2.3) with $n_1 = .8$, $n_2 = .2$ and $\lambda = 10.6 \mu$ are given in Fig. 2.3. The values predicted by the Mie code are shown for comparison. Three limiting cases are also plotted; they are (1) the Rayleigh limit

$$F = - \frac{8\pi R}{\lambda} \operatorname{Im} \left(\frac{n^2 - 1}{n^2 + 2} \right),$$

where $n = n_1 - i n_2$, (2) the surface absorber limit

$$F = n_1^2,$$

and (3) the volume absorber limit

$$F = \frac{4R}{3} n_1^2 \alpha.$$

The Mie code approaches the Rayleigh limit for small R , thereby suggesting that the code is reliable even for $n_1 < 1$. The ray optics prediction approaches the surface absorption limit for large R and volume absorption limit for small R . This behavior for small R is the correct mathematical limit for ray theory, but is not the correct limit for the physical phenomenon since the requirement $\lambda \ll R$ is no longer met. In the regime of interest, $R = 15 \mu$, ray theory predicts 61% absorption whereas Mie theory predicts 87% absorption.

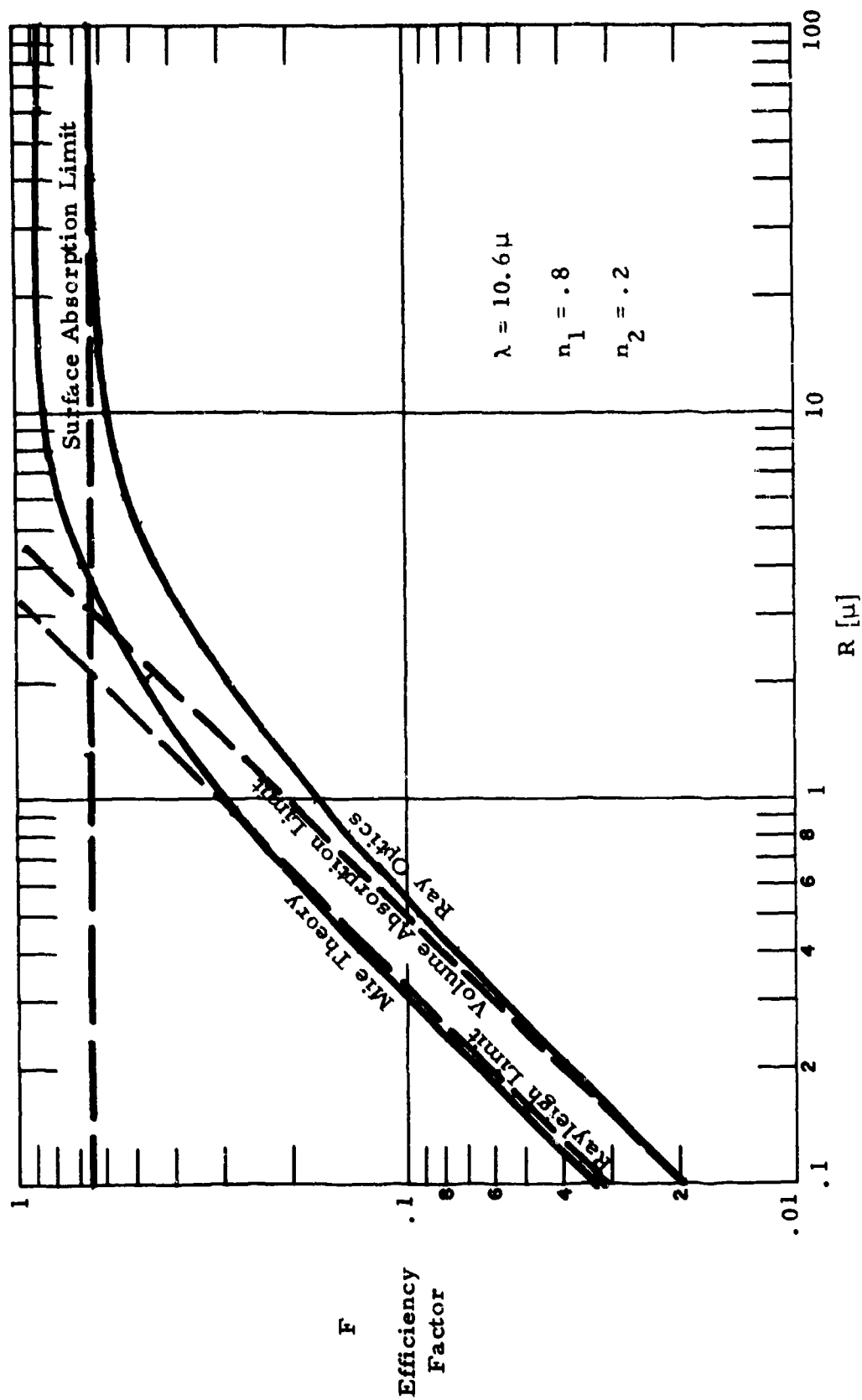


Fig. 2.3 Fraction of the 10.6μ Laser Intensity which is Absorbed by a Sphere of Radius R having an Index of Refraction of $.8 - .2i$.

The value from Mie theory will be used for calculations which require only the total energy absorbed. For calculations concerned with local energy deposition the ray theory predictions will be used to suggest the maximum energy deposition rates within the particle. The assumption we make in this approach is that the enhanced absorption of Mie theory comes from stronger absorption in regions where ray theory does not predict much absorption, whereas the maximum absorption rates which generally prevail are unaltered.

The discrepancy between the two theories suggests that calculations accurate to better than 30% require a complete analysis using full Mie theory to study deposition. Such an ambitious project should not be undertaken, however, without also understanding how to incorporate the effects of both spatial variations of the index of refraction (caused by non-uniform heating) and non-uniform surface recession (caused by vaporization). (Of course many other factors, such as particle motion, which are neglected in this report, are also important for more accurate calculations.)

Prediction of the time when vaporization commences requires information about local energy deposition. We can qualitatively study local deposition via ray theory. In Fig. 2.4 several rays are shown striking an Al_2O_3 particle. The path of the ray directed towards the center is not changed, therefore the energy deposition along its path is proportional to $\alpha e^{-\alpha z}$ where z is the distance along the ray from the front surface. Two competing processes influence the deposition rate at other interior points. The convex shape of the interface causes rays to diverge after passing into the particulate, hence the intensity in the interior drops faster than $e^{-\alpha z}$ due to the geometric spreading. On the other hand, the initial effect of the change in direction on passing through the interface is to squeeze the rays together, thereby creating a more intense beam. Therefore, at the surface, the intensity, and hence the absorption per unit volume, is enhanced. The numbers in Fig. 2.4 associated with each ray in the relative intensity immediately inside the particulate. The numbers along the central

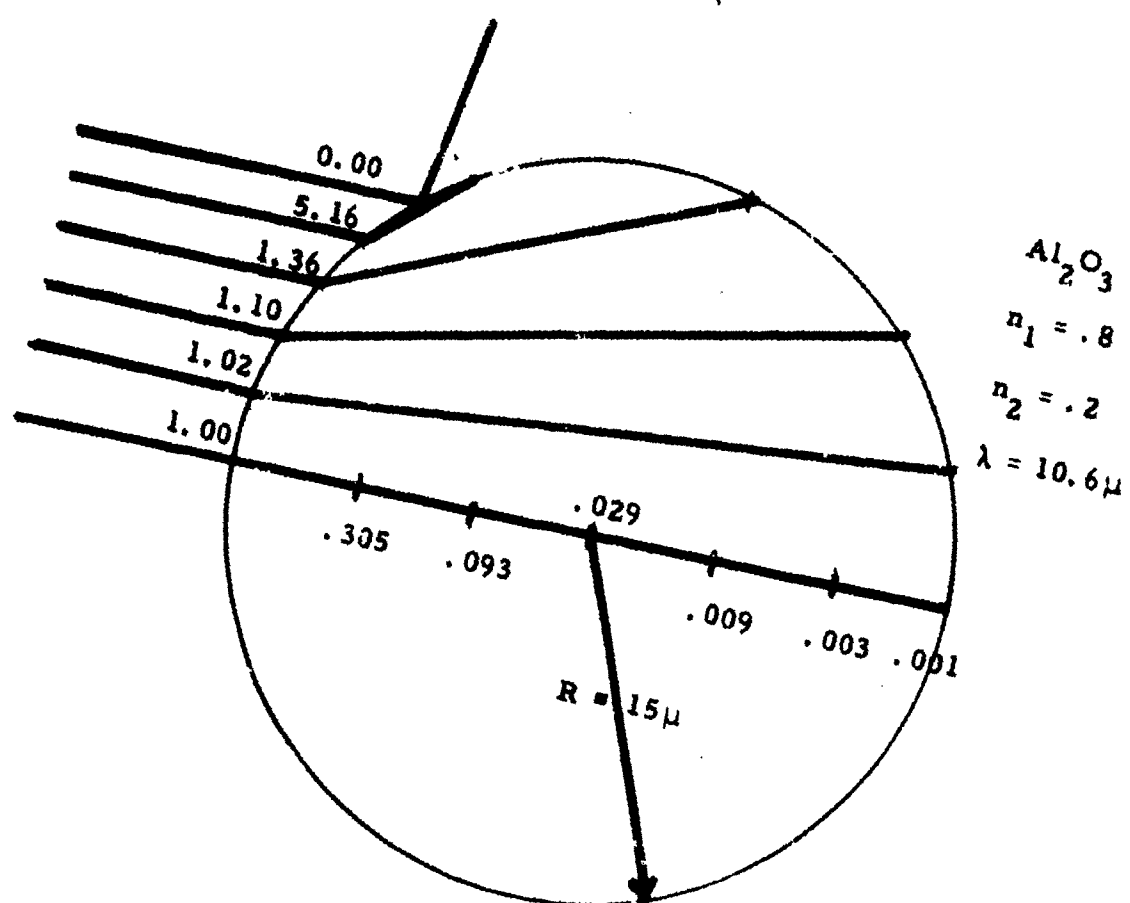


Fig. 2.4 Typical Rays Passing Through a Sphere of Al_2O_3
 The number refer to the relative intensity of the
 radiation in the particulate.

ray represent the intensity at interior points if defocussing is neglected. It is evident that "hot spots" exist where energy is absorbed much more quickly than over the rest of the surface. The bulk of the particle surface, however, absorbs at a rate only minimally above the absorption rate for the central ray. Therefore bulk heating is characterized by $\propto I_0$.

The final ingredients needed to predict vaporization time scales are the thermodynamic properties of Al_2O_3 in its various forms. The JANAF¹⁵ tables were used as sources of melting temperature, specific heat, free energy and enthalpy of formation for solid Al_2O_3 , liquid Al_2O_3 and the vapor components AlO , AlO_2 , Al_2O , Al_2O_2 , O_2 , O_3 , AlO^+ , Al_2O^+ , Al_2O_2^+ , O^- , O_2^- and Al_2O_2^- . The energy levels and degeneracies of Moore¹⁶ were used for the atomic species - Al , Al^+ , Al^{++} , O and O^+ . The vapor pressure above the Al_2O_3 liquid surface at any temperature T was determined by an equilibrium code calculation which solves the equations relating species concentrations in thermodynamic equilibrium. A plot of vapor pressure versus T is given in Fig. 2.5, along with the enthalpy of the vapor. The boiling point is thus determined to be 4000°K and the heat of vaporization at 4000°K is found to be $2.02 \times 10^6 \text{ J/mole}$. It can be seen from Fig. 2.5 that the enthalpy per unit mass does not change appreciably over the temperature range displayed. A summary of useful thermodynamic properties of Al_2O_3 is given in Table 2.2. Thermal conductivity and density were taken from the AIP handbook.¹⁷

The time τ_v at which the surface begins to vaporize is given by

$$\tau_v = \rho \Delta h / \alpha I_0 \quad (2.4)$$

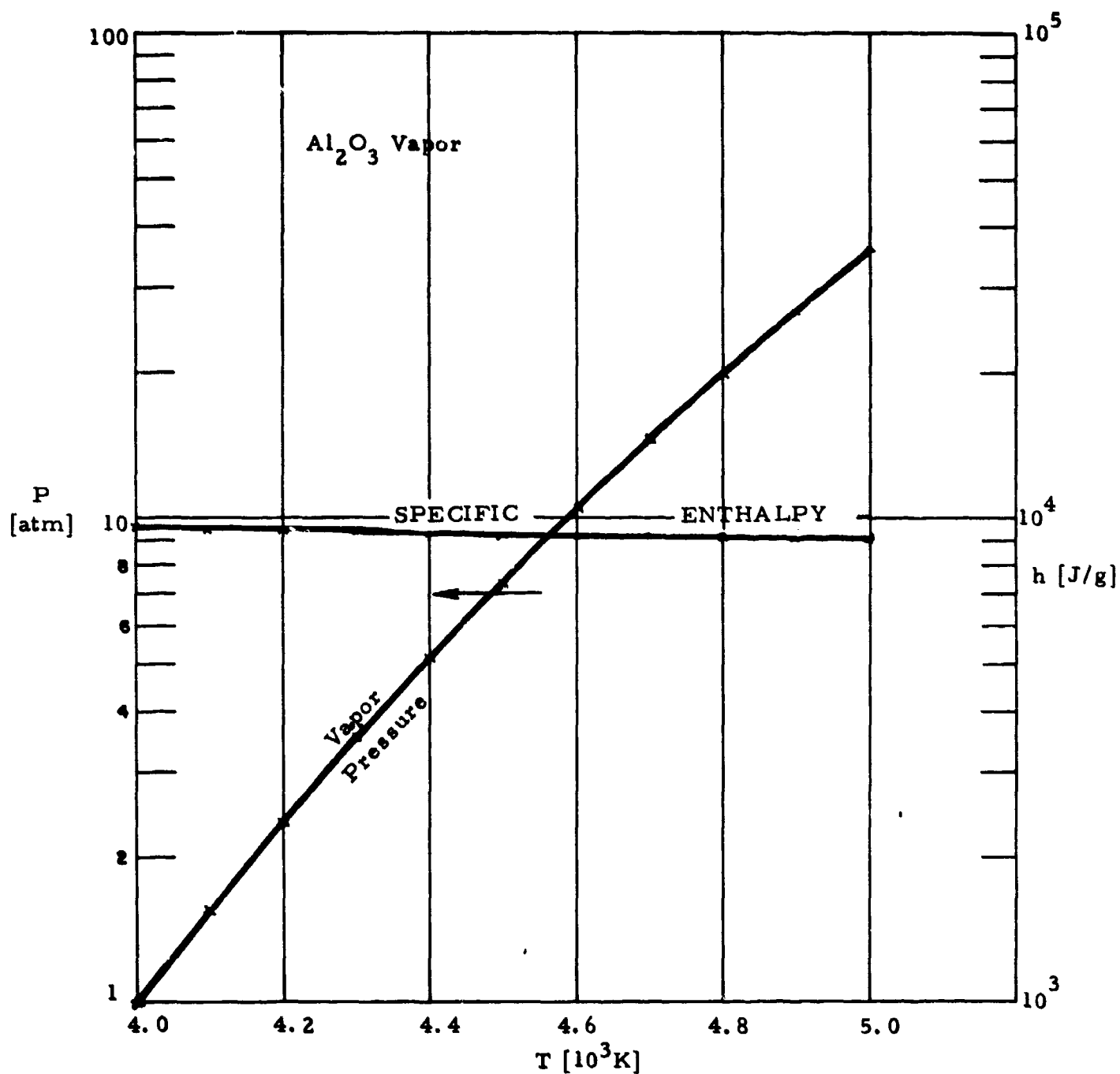


Fig. 2.5 Vapor Pressure and Specific Enthalpy of Al_2O_3 vapor in Equilibrium with Liquid Al_2C_3 .

TABLE 2.2
Properties of Al_2O_3 Used in Calculation

Quantity	Symbol	Value	Ref.
Density	ρ	3.8 g/cc	17
Specific heat (average)	c_p	1.4 J/gK	15
Atomic weight	A	101.96	15
Thermal conductivity (average)	λ_c	.1 W/cm K	17
Melting temperature	T_m	2315 K	15
Normal boiling point	T_v	400 K	equilibrium code
Heat of fusion	h_m	$\left\{ \begin{array}{l} 1.19 \times 10^5 \text{ J/mole} \\ 1.67 \times 10^3 \text{ J/g} \\ 4.43 \times 10^3 \text{ J/cm}^3 \end{array} \right\}$	15
Heat of vaporization	h_v	$\left\{ \begin{array}{l} 2.02 \times 10^6 \text{ J/mole} \\ 1.98 \times 10^4 \text{ J/g} \\ 7.53 \times 10^4 \text{ J/cm}^3 \end{array} \right\}$	equilibrium code
Enthalpy difference between gas at 4000°K and 1 atm and solid at 300°K	Δh	$\left\{ \begin{array}{l} 2.63 \times 10^6 \text{ J/mole} \\ 2.58 \times 10^4 \text{ J/g} \\ 9.8 \times 10^4 \text{ J/cm}^3 \end{array} \right\}$	$\left\{ \begin{array}{l} \text{equilibrium code} \\ \text{and} \\ 15 \end{array} \right\}$
Real part of index of refraction (average)	n_1	.8	10
Imaginary part of index of refraction	n_2	.2	10
Bulk absorption coefficient, $\lambda = 10.6 \mu$	α	2370 cm^{-1}	

where ρ is the solid density and Δh is the energy required to change Al_2O_3 from a solid at room temperature to a vapor at the vapor temperature. For the purposes of this calculation Al_2O_3 is assumed to vaporize directly into the equilibrium vapor constituents. It is shown in Fig. 2.5 that the enthalpy of the vapor does not change appreciably as the vapor temperature is raised. Therefore a constant value of $\Delta h = 2.63 \times 10^6$ J/mole $= 2.58 \times 10^4$ J/g is used to calculate τ_v . This corresponds to a vapor pressure of one atmosphere and a vapor temperature of 4000°K . We find for $\lambda = 10.6\mu$ that the fluence required to vaporize the surface is

$$I_0 \tau_v = 41.4 \text{ J/cm}^2, \quad (2.5)$$

where I_0 is the incident laser flux. In the range of intensity of interest, bulk vaporization commences from 5 to 14 microseconds after start of the pulse. As an aside it should be noted that the requirement of 41 J/cm^2 to cause bulk vaporization does not conflict with the observed breakdowns shown in Fig. 1.1 which occur with only 10 J/cm^2 fluence. These observations are made at high intensities where bulk vaporization is not required to initiate breakdown. Indeed, the "hot spots" mentioned earlier vaporize before 10 J/cm^2 is received and their vaporization may be sufficient to induce breakdown at high intensity.

The calculation neglected thermal conduction within the particulate and conduction losses at the surface to the air. The losses to the air are minimal. As will be shown in the Section 3.5 the flux at the surface into the air at time t is given by

$$q = \frac{\lambda \Delta T}{R} \left\{ 1 + \sqrt{\frac{R}{\pi K t}} \right\}, \quad (2.6)$$

where λ is the thermal conductivity of air (5.85×10^{-3} W/cmK at 4000°K and one atmosphere), ΔT is the temperature difference between the surface and the initial air temperature and K is the thermal diffusivity of air ($32.8 \text{ cm}^2/\text{sec}$ at 4000°K and one atmosphere). The maximum flux occurs when the liquid reaches the vaporization temperature, but before any of the heat of vaporization is added. For $T = 4000^\circ\text{K}$, $I_0 = 5 \times 10^5 \text{ W/cm}^2$, $\Delta T = 3700 \text{ K}$, this time is given by $t \sim 9.6/I_0 = 2 \mu\text{sec}$. Then $q = 1.6 \times 10^4 \text{ W/cm}^2$ is the maximum flux expected to be lost through conduction to the air. However the rate of energy deposition immediately below the surface is $\alpha I = 1.2 \times 10^{10} \text{ W/cm}^2$. Clearly the conduction losses can be supplied by the energy deposited in a very thin surface layer.

A potentially more serious effect is thermal conduction within the particle. The thermal diffusivity for Al_2O_3 is found from Table 2.2 to be $1.8 \times 10^{-2} \text{ cm}^2/\text{sec}$. If thermal conduction is ineffectual, the temperature profile at time t is given by

$$T(z) = \frac{I_0 t \alpha e^{-\alpha z}}{\rho c_p}$$

where z is the distance from the surface. For this profile, the local source term due to thermal conduction is

$$\lambda \frac{d^2 T}{dz^2} = \alpha^3 I_0 t e^{-\alpha z} K = S_{TC}$$

which is to be compared to the source term due to laser absorption $S_L = \alpha I_0 e^{-\alpha x}$. Their ratio is

$$S_{TC}/S_L = \alpha^2 K t$$

As before the time over which the sources are to be compared is the time required to reach the vaporization temperature. For $I_0 = 3 \times 10^6 \text{ W/cm}^2$ the time is $3 \times 10^{-6} \text{ sec}$ which leads to a ratio of .3. Therefore, even at its maximum value, thermal conduction is small compared to laser heating.

Having established the shortest time for bulk vaporization to occur, we now characterize the time to vaporize a given fraction β of the particle. In developing a simple model for this process we assume that all the absorbed energy is effective in vaporizing the particulate. Under the further assumption that the absorption cross section does not change significantly during vaporization we find the relationship

$$t_\beta I_0 \pi R^2 F = \beta \rho \Delta h \frac{4\pi R^3}{3} \quad (2.7)$$

where, as before F is the efficiency factor and Δh is the energy required. For a 15μ particle of Al_2O_3 with $F = .87$, the time to change a fraction β of the particle to vapor at one atmosphere and 4000°K is given by

$$I_0 t_\beta = 225 \beta \text{ J/cm}^2 \quad (2.8)$$

Of course for small β the prediction is obviously incorrect - vaporization has not begun. In the limit of small β the correct time is the sum of t_β and τ_v . The approximation should be reliable as β approaches one, however, since then all the absorbed energy then contributes to the vaporization. The time as predicted by Eq. (2.7) is tabulated in Table 2.3 for three values of I_0 and three values of β . Clearly a major portion of the observed breakdown time is spent producing the vapor. It should be kept in mind that the times predicted by Eq. (2.7) are only rough estimates. It is not known how the energy absorbed changes once vaporization begins to change the geometry of the particulate.

TABLE 2.3

Characteristic Times for Vaporization of a Al_2O_3 Particle
 $R = 15 \mu$

I_o [W/cm ²]	τ_v [μ sec]	$\tau_{.125}$ [μ sec]	$\tau_{.658}$ [μ sec]	$\tau_{1.00}$ [μ sec]
3×10^6	13.8	9.4	49.4	75
5×10^6	8.3	5.6	29.6	45
8×10^6	5.2	3.5	18.5	28

τ_v = time vaporizations commences

τ_β = time to vaporize a fraction β of the particle

The second stage of the breakdown process presupposes a pure cloud of the vapor exists. However, a pure cloud cannot be formed unless the vaporization rate is much faster than the rate at which the vapor can diffuse into the air. It is common to assume that a pure cloud will be formed if the pressure of the vapor at the particle surface is above two or three atmospheres. An estimate of the pressure of the vapor at the interface can be made as follows: The mass flux is determined by the heating rate. In the limit of one-dimensional steady state recession the mass flux per unit area $\rho_s u_s$ is related to the laser intensity, which is assumed to be entirely absorbed, by

$$\rho_s u_s \Delta h = I_0 ,$$

where, as before, Δh is the enthalpy required to change a solid to a vapor at the required conditions. The temperature and vapor pressure are related as shown in Fig. 2.5. For the present estimates, a constant value of $\Delta h = 2.63 \times 10^6$ J/mole can be used. Under the assumption that there is massive vaporization, the velocity of the vapor, denoted by u_v , assumes its limiting value, the sonic velocity, which defined by

$$u_v = \sqrt{\gamma R T} ,$$

where R is the ideal gas constant and γ is the ratio c_p/c_v . Furthermore, using both mass continuity at the interface,

$$\rho_s u_s = \rho_v u_v ,$$

where ρ_v is the vapor density, and the ideal gas law,

$$p = \rho_v R T ,$$

we obtain the approximate relationship

$$p = \frac{I_o}{\Delta h} \sqrt{\frac{RT}{Y}} \quad (2.9)$$

or

$$p [\text{atm}] = 8.2 \times 10^{-7} I_o [\text{W/cm}^2] \quad (2.10)$$

Equation (2.9) is expected to predict reasonable values of the pressure whenever steady state recession is approached. Immediately after vaporization commences, the pressure is higher than the steady state value, but for the time scale required to obtain appreciable vaporization the steady state pressure is representative of the average pressure.

Several values of p as determined by Eq. (2.10) are given in Table 2.4. The equation breaks down for low pressures because u_v is no longer the sonic velocity. It should hold, however, for the pressures of interest, that is, for pressures greater than two or three atmospheres. From Eq. (2.10) then, a reasonable threshold intensity for production of a pure vapor is $3 \times 10^6 \text{ W/cm}^2$. This criteria agrees well with the observed threshold, which suggests that a pure vapor cloud is indeed needed.

The pressure calculation does not involve the particle radius; it only demands that the particle be large enough to justify the assumption of steady state recession. Therefore a lower limit has been calculated which is valid for the production of a pure Al_2O_3 vapor over even a semi infinite plane. If breakdown does indeed require a pure cloud, then large particles should have the same intensity threshold as the 30μ diameter particles of Al_2O_3 .

To summarize, the rough estimates of the time to the start of vaporization, the time to vaporize an arbitrary fraction of the particle, and the vapor pressure above the interface are consistent with experimental observations of the delay time. Furthermore, it has been shown that the threshold for

TABLE 2.4

Pressure as a Function of 10.6μ Laser Intensity for
 Al_2O_3 - Assuming Steady State Recession and Rapid Vaporization

I_o [W/cm^2]	p [atm]	T_{vapor} [K]
10^6	.82	3960
2×10^6	1.6	4110
3×10^6	2.5	4210
4×10^6	3.3	4280
5×10^6	4.1	4340
6×10^6	4.9	4390
7×10^6	5.7	4430
8×10^6	6.6	4470

production of pure Al_2O_3 vapor is about $3 \times 10^6 \text{ W/cm}^2$ for 10.6μ radiation. Finally the time required to produce the vapor cloud is a significant portion of the delay time observed before breakdown.

The final subject to be discussed in this section is how these predictions for vapor production change as the laser wavelength and particle composition are altered. For the calculation of τ_v the important quantities are the energy required to vaporize a unit volume, $\rho \Delta h$, and the energy deposition rate per unit volume, denoted by αI . It is important that the maximum value of αI be used. For $\alpha R \gg 1$ the maximum occurs at the front surface, but for $\alpha R \ll 1$ the maximum value may occur at the back of the particle because of focusing effects. SiO_2 particles may show this effect. The time to vaporize a given fraction β of the particle is once again given by Eq. (2.7). Only the composition of the particulate affects $\rho \Delta h$, but both the composition and the wavelength affect F . The pressure of the vapor is related only to the composition, under the assumption that the recession rate is steady. This assumption, however, is valid only if the laser energy is absorbed reasonably close to the surface; therefore the applicability of Eq. (2.9) depends upon laser wavelength as well as composition. As a final comment, it should be noted that Al_2O_3 has a small imaginary index of refraction at short wavelengths. In fact, at 3.8μ , the bulk absorption coefficient is of the order of $.3 \text{ cm}^{-1}$ rather than 2370 cm^{-1} . The particle is effectively transparent and does not vaporize. Long pulse Al_2O_3 induced breakdown at 3.8μ will not occur at the intensities studied here, although it may still occur at these intensities for other particulates.

3. VAPOR CLOUD HEATING

The second stage of the long pulse breakdown process is the heating of the vapor cloud by the laser. In this section two simple models are used to estimate both the time to heat the vapor to $20,000^{\circ}\text{K}$ and the threshold intensity below which the vapor will not heat. One model is appropriate for short times; it assumes that the vapor in the center of the cloud is effectively insulated from the cold air by the outer layers of vapor. The other model is appropriate for longer times and slow heating. Thermal conduction is able to establish a temperature profile wherein the losses are effectively distributed over the complete vapor cloud. In both models the heating is assumed to occur slowly enough that the pressure remains constant and the composition of the vapor cloud is determined by thermodynamic equilibrium. The constant pressure assumption is reasonable since the heating is known to take several microseconds, whereas the characteristic time for equilibrating pressure is of the order of .3 microseconds. The chemical equilibrium assumption, at least in the beginning stages, involves the rate of dissociation of molecules. Characteristic times for establishing chemical equilibrium at $4,000^{\circ}\text{K}$ are also expected to be less than a microsecond.

3.1 Initial Conditions

Before the models can be exercised the initial conditions must be determined. Since the pressure equilibrates with the surrounding air within .3 microseconds, the vapor cloud starts (and remains) at one atmosphere. The initial temperature is then expected to be near 4000°K - otherwise the vapor should liquify. A more accurate estimate of the initial temperature can be calculated as follows: Given a value of the incident laser intensity I_0 ,

3. VAPOR CLOUD HEATING

The second stage of the long pulse breakdown process is the heating of the vapor cloud by the laser. In this section two simple models are used to estimate both the time to heat the vapor to $20,000^{\circ}\text{K}$ and the threshold intensity below which the vapor will not heat. One model is appropriate for short times; it assumes that the vapor in the center of the cloud is effectively insulated from the cold air by the outer layers of vapor. The other model is appropriate for longer times and slow heating. Thermal conduction is able to establish a temperature profile wherein the losses are effectively distributed over the complete vapor cloud. In both models the heating is assumed to occur slowly enough that the pressure remains constant and the composition of the vapor cloud is determined by thermodynamic equilibrium. The constant pressure assumption is reasonable since the heating is known to take several microseconds, whereas the characteristic time for equilibrating pressure is of the order of .3 microseconds. The chemical equilibrium assumption, at least in the beginning stages, involves the rate of dissociation of molecules. Characteristic times for establishing chemical equilibrium at $4,000^{\circ}\text{K}$ are also expected to be less than a microsecond.

3.1 Initial Conditions

Before the models can be exercised the initial conditions must be determined. Since the pressure equilibrates with the surrounding air within .3 microseconds, the vapor cloud starts (and remains) at one atmosphere. The initial temperature is then expected to be near 4000°K - otherwise the vapor should liquify. A more accurate estimate of the initial temperature can be calculated as follows: Given a value of the incident laser intensity I_0 ,

the vapor temperature T_v and the pressure p_v of the vapor at the surface of the particulate are found from Fig. 2.5 and Eq. (2.10) respectively. The vapor expands to one atmosphere in a fraction of a microsecond. Therefore, the laser heating during the expansion should be negligible and the initial temperature T_s of the vapor cloud corresponds to isentropic expansion of the vapor from p_v and T_v to one atmosphere and T_s . A plot of T_s versus p_v for Al_2O_3 , as determined by the equilibrium code, is given in Fig. 3.1. Of particular interest are the values $3940^\circ K$ and $3870^\circ K$ which are reached when the laser intensities are $3 \times 10^6 W/cm^2$ and $8 \times 10^6 W/cm^2$ respectively. These values straddle the interesting range of intensity. Since the values of T_s lie so close to the normal boiling point the calculations performed in this section are made with a constant initial temperature of $4000^\circ K$. For completeness, however, the various physical parameters are evaluated for temperatures as low as $3500^\circ K$. The last parameter to be determined is the initial vapor cloud size. A fraction β of a Al_2O_3 particle which is 15μ in radius produces a vapor cloud at $4000^\circ K$ and one atmosphere which has a radius of $352(\beta)^{1/3}$ microns.

3.2 Physical Parameters Required by the Models

The local equation governing the temperature history of the vapor is

$$\rho(T) c_p(T) \frac{\partial T}{\partial t} = \kappa_L'(T) I_0 - \vec{\nabla} \cdot \vec{S} - \vec{\nabla} \cdot \lambda_c(T) \vec{\nabla} T \quad (3.1)$$

where ρ is the density, c_p the specific heat, κ_L' the effective laser absorption coefficient, \vec{S} the radiative flux produced by the vapor and λ_c the coefficient of thermal conductivity. Approximations for $\vec{\nabla} \cdot \vec{S}$ and $\vec{\nabla} \cdot \lambda_c \vec{\nabla} T$, which are made later in this section, depend upon the vapor cloud radius $R(T)$. The use of the incident laser intensity I_0 throughout the entire volume assumes that the cloud is transparent to laser radiation. The

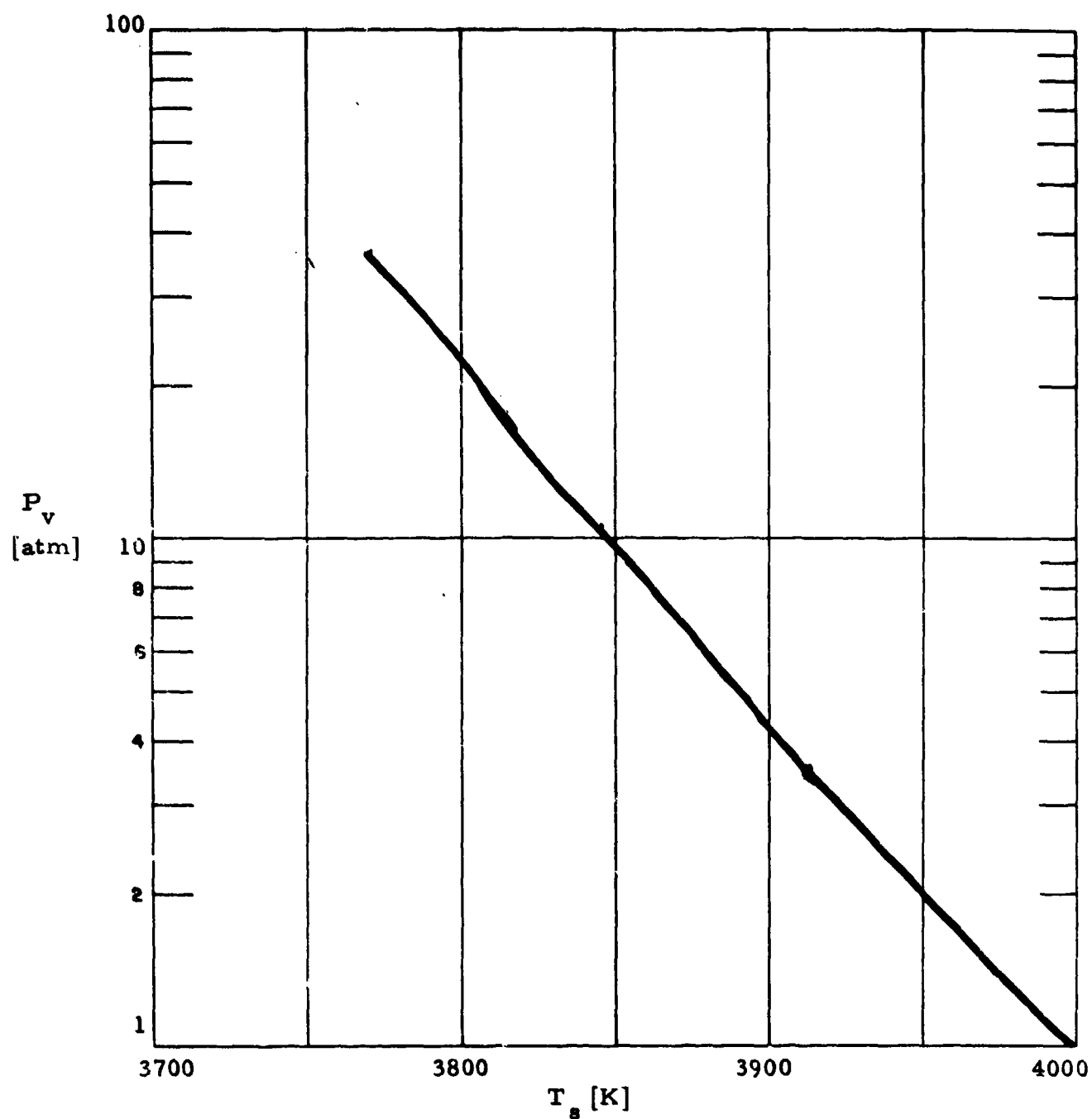


Fig. 3.1 The Relationship Between the Pressure of a Al_2O_3 Vapor Cloud in Equilibrium with Liquid Al_2O_3 and the Temperature of the Vapor after Isentropic Expansion to One Atmosphere.

values of κ_L' and R determined in the following subsections justify this simplification. In the subsequent subsections, the physical parameters ρ , c_p , $R(T)$, $\kappa_L'(T)$ and $\lambda_c(T)$ are discussed, and the models for $\vec{\nabla} \cdot \vec{S}$ and $\vec{\nabla} \cdot \lambda_c \vec{\nabla} T$ are described.

3.3 Parameters Determined by the Equilibrium Code

The equilibrium code gives the density, enthalpy and specific heat of the vapor in addition to the concentrations of the various species. In Fig. 3.2 we plot the product ρc_p . The large values at low temperature indicate that a large fraction of the total energy must be supplied in the initial heating. In Figs. 3.3 and 3.4 the mole fraction of the various species are shown. Figure 3.3 gives the composition for low temperature where many molecular species are present and rapid variations in the composition occur within a few hundred degrees. Figure 3.4 displays the relative concentration of ions, electrons and atoms over the complete range of temperature of interest. The density of the vapor can be used to determine the radius of the vapor cloud. In Fig. 3.5 the radius is given as a function of temperature for three values of β .

3.4 Laser Absorption Coefficient

Two types of transitions can absorb laser radiation: free-free transitions of electrons during collisions with heavy particles, and molecular transitions between states of different vibrational and rotational quantum numbers. The electron transitions - called inverse Bremsstrahlung - absorb for any wavelength of laser and their absorption cross section scales roughly as wavelength squared. Molecular transitions, on the other hand, occur over limited frequency bands, and a change of laser wavelength may strongly enhance the absorption or eliminate it entirely.

The inverse Bremsstrahlung absorption coefficient is given by

$$\kappa_L' = (1 - e^{-1.43883 \omega/T}) \sum Q_i n_i n_e \quad (3.2)$$

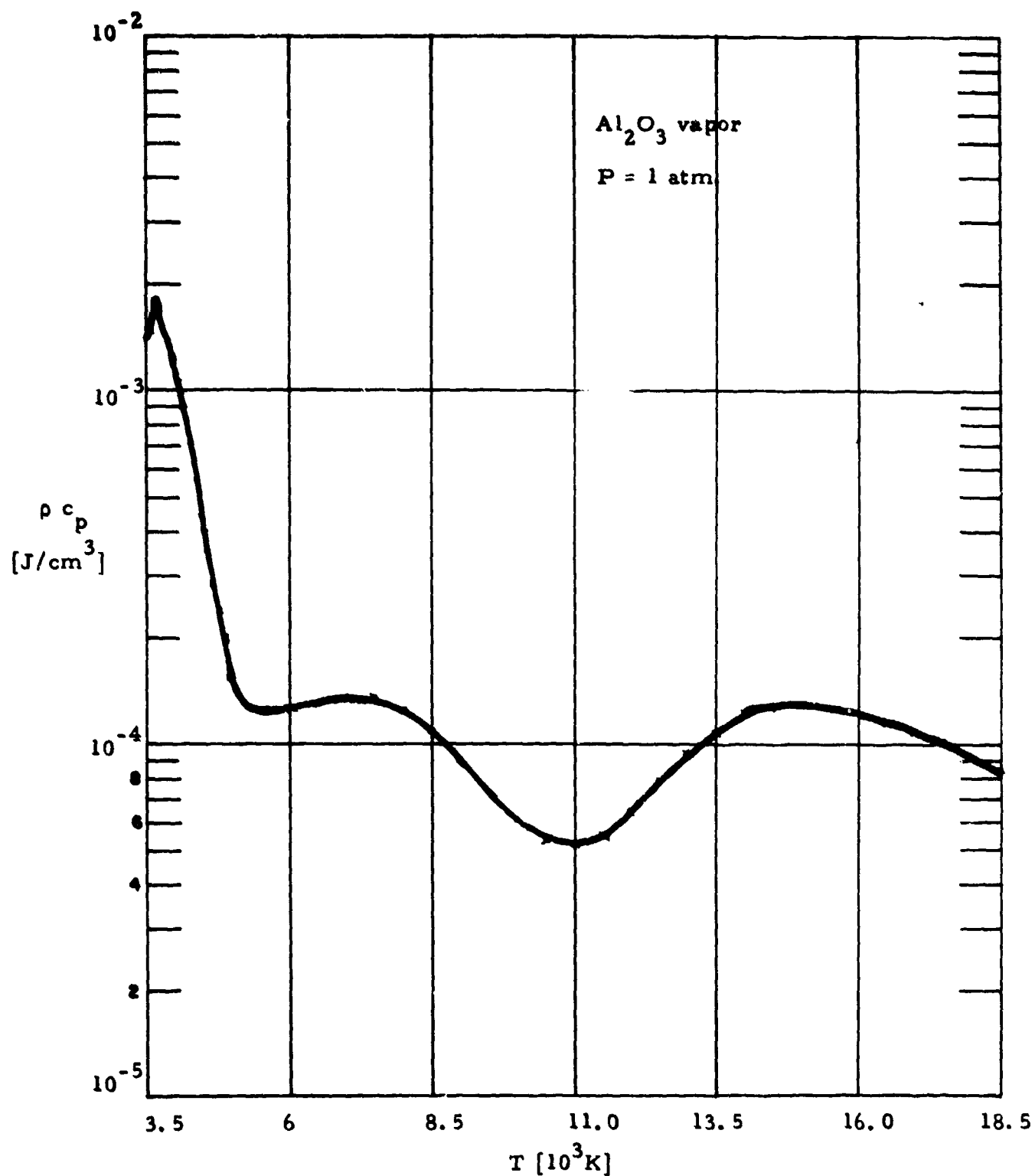


Fig. 3.2 Specific Heat Per Unit Volume of Al₂O₃ Vapor in Thermodynamic Equilibrium at One Atmosphere.

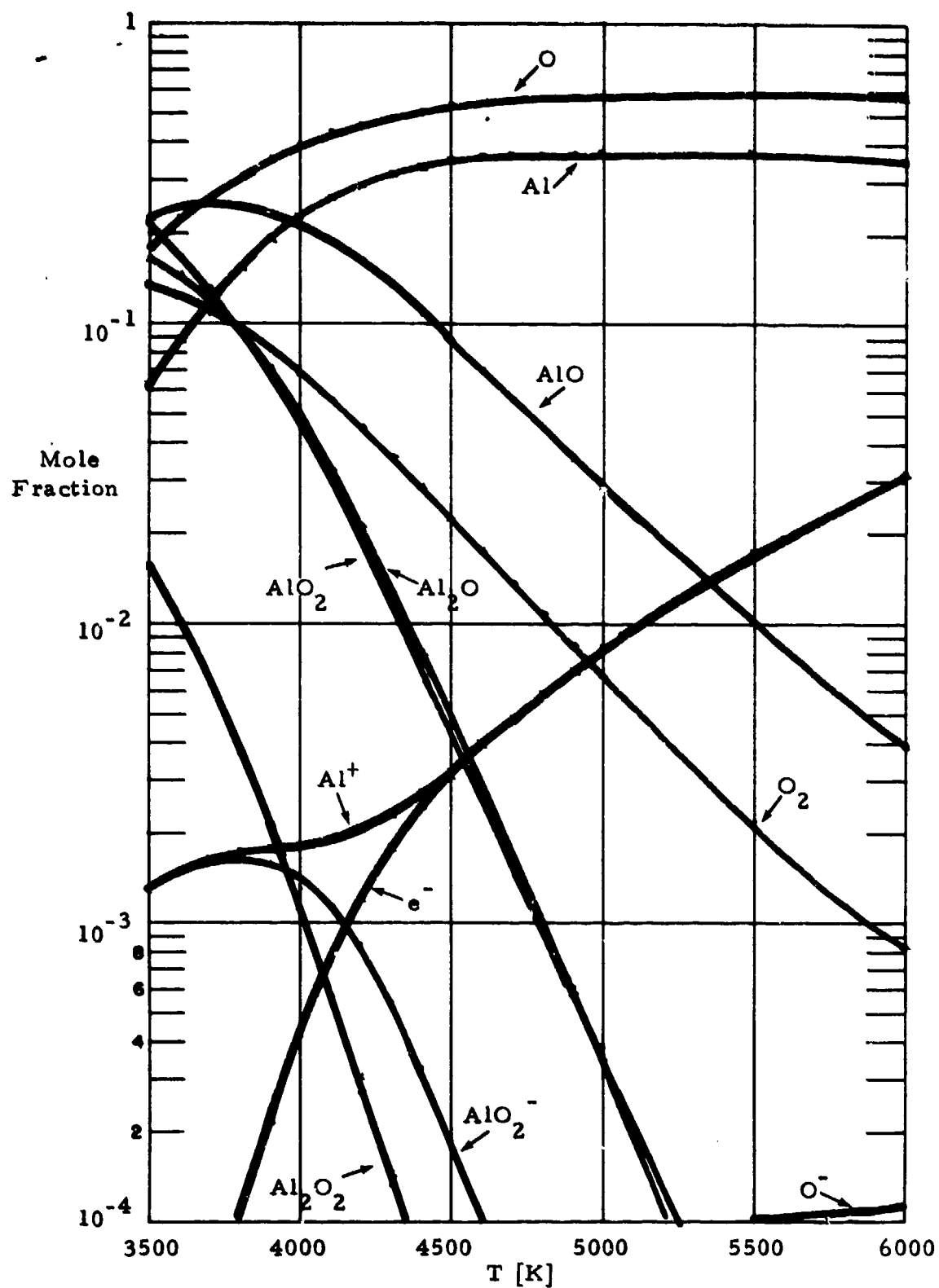


Fig. 3.3 Equilibrium Composition of Al_2O_3 Vapor at One Atmosphere Pressure.

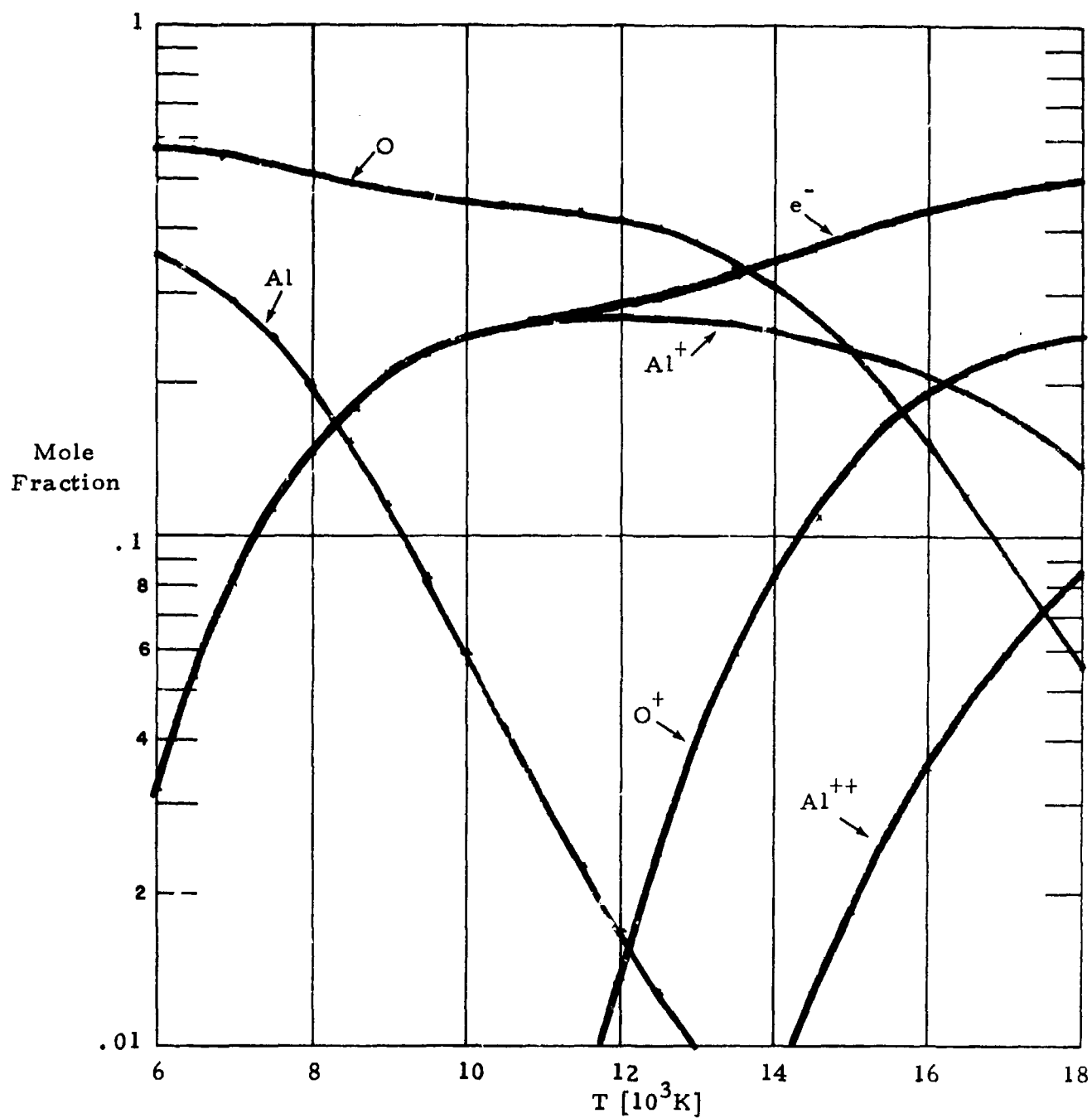


Fig. 3.4 Atomic and Ionic Composition of Al_2O_3 Vapor at One Atmosphere.

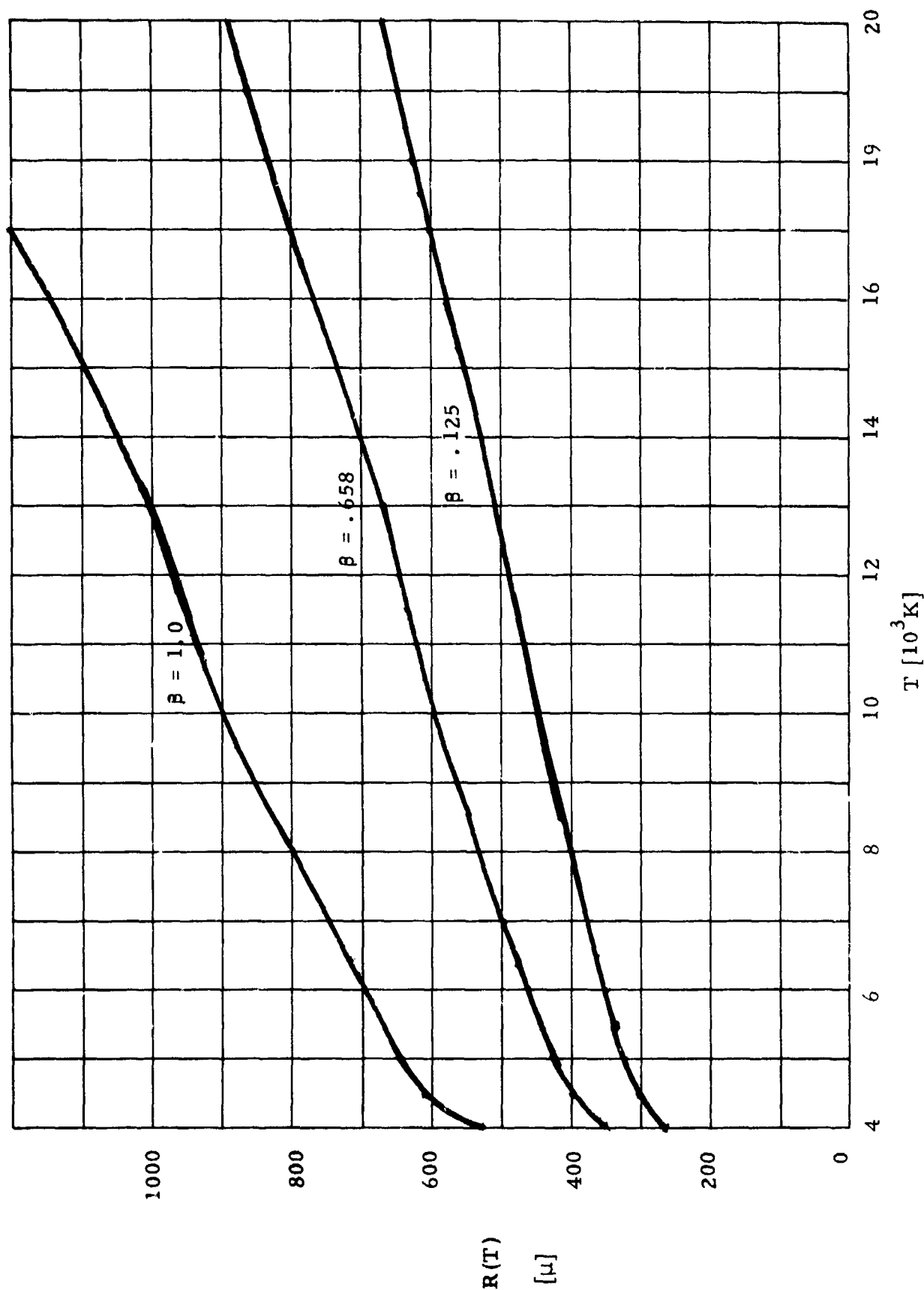


Fig. 3.5 Radius of the Vapor Cloud at One Atmosphere Formed from a Fraction β of a Al_2O_3 Particulate which has a Radius of 15μ .

where ω is the wave number of the laser radiation in cm^{-1} , T is the temperature in $^{\circ}\text{K}$, n_e is the concentration of electrons, n_i the concentration of the i^{th} species and Q_i the average cross section for absorption of a photon of wavenumber ω by an electron colliding with a particle of species i . For charged species the cross section can be approximated by the product of the Gaunt factor \bar{g} , given by Karzas and Latter,¹⁸ and the semiclassical formula of Kramer:¹⁹

$$Q_i = \frac{4}{3} \bar{g} \left(\frac{2\pi}{3 m_e kT} \right)^{1/2} \frac{e^6 Z_i^2}{c^4 m_e h_p \omega^3} \quad (3.3)$$

where ω is the wave number of the radiation, m_e is the mass of the electron, h_p is Planck's constant, k is Boltzmann's constant, e is the charge of the electron, c is the velocity of light and Z_i is the charge of the particle in units of electron charge.

The cross section of the neutral species is not accurately known although typical values are of the order of 10^{-36} cm^5 . We used the following estimates of Q for the neutral species. For Al, a highly polarizable atom, the expression of Hyman and Kivel²⁰ and the polarizability given by Teachout and Pack²¹ were used to predict the cross section

$$Q_{\text{Al}} = .64 (T/10^3)^{10^{-36}} \quad (3.4)$$

The cross sections for O and O_2 were deduced from the experimental values given by Taylor and Caledonia.²² All others were guessed by using the predictions for Al, O and O_2 as guides. The cross sections used herein are listed in Table 3.1. The prediction of neutral and charge inverse Bremsstrahlung absorption coefficients for 10.6μ radiation and equilibrium Al_2O_3 vapor at one atmosphere are plotted in Fig. 3.6. The total inverse Bremsstrahlung absorption coefficient is shown as well. The rapid increase of κ_L' with the temperature suggests that the initial heating of the vapor accounts for most of the time consumed in the vapor heating stage. Electron-neutral inverse Bremsstrahlung dominates in the low temperature regime.

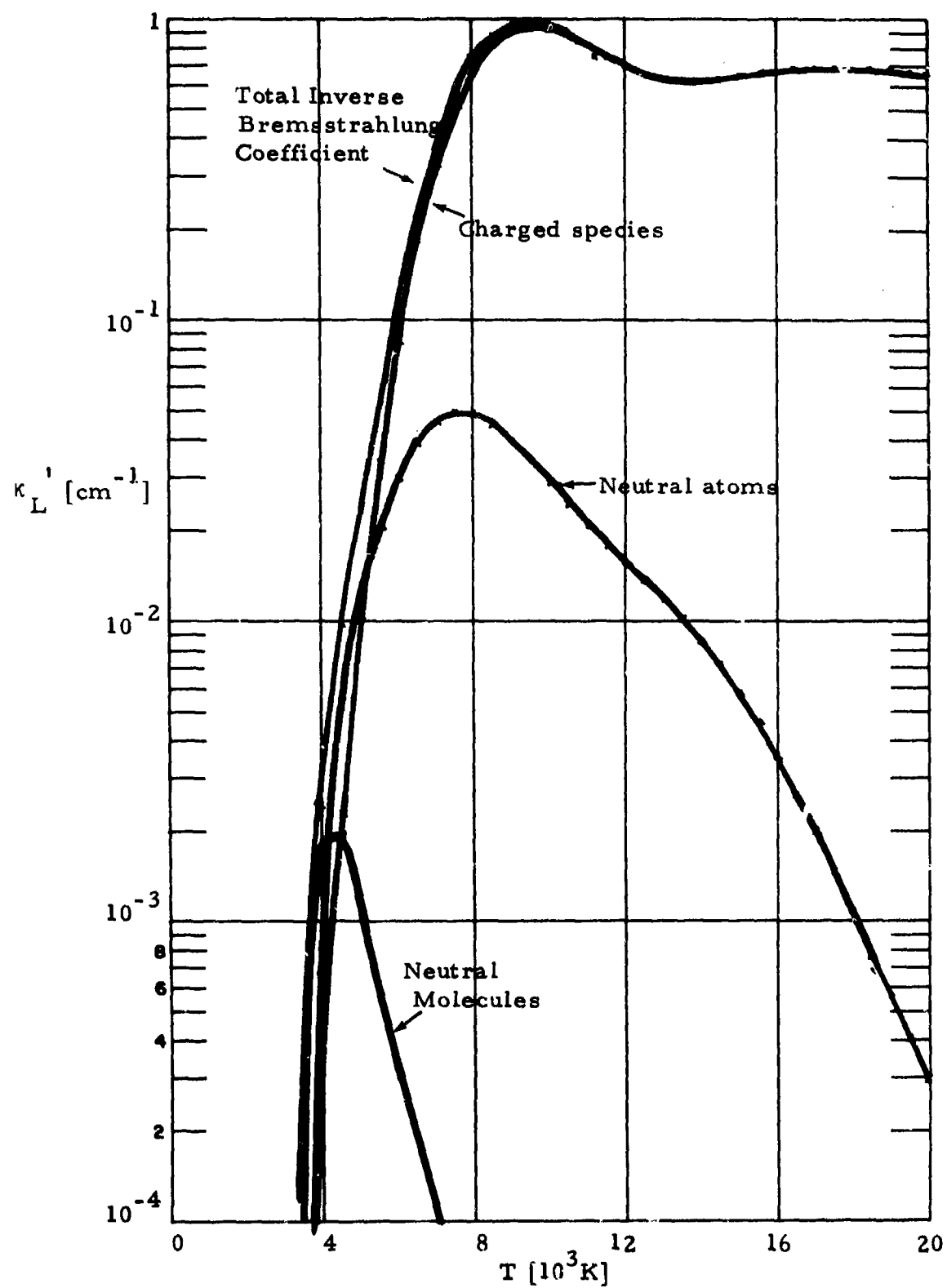


Fig. 3.6 Laser Absorption Coefficient from Inverse Bremsstrahlung.

TABLE 3.1

Species	Estimated Q for 10.6 μ Radiation [cm ⁵]
Al	$.64 (T/10^3) 10^{-36}$
O	3×10^{-36}
O ₂	1.2×10^{-35}
AlO	6×10^{-36}
Al ₂ C	1.2×10^{-35}
AlO ₂	1.2×10^{-35}
Al ₂ O ₂	1.2×10^{-35}

The other mechanism whereby 10.6 μ radiation can be absorbed in molecular absorption. Among the molecular species in Al_2O_3 vapor only AlO has its vibration-rotation band near 10.6 μ . In order to estimate the absorption accurately the precise wave number of the laser line is required. The laser used in breakdown experiments lases mainly on the P(20) line of CO_2 , although it often fires on the P(18) and P(22) line also.²³ The wave numbers of these lines, as given by McClatchy and Selby²⁴ are listed in Table 3.2. For the temperature and pressure of interest the lines of the AlO vibration-rotation transitions are narrow; therefore the absorption coefficient must be calculated by summing the contributions of individual lines rather than by using an overlapping line model. We used the following method to compute the absorption. The energy levels of the $\text{AlO } X^2\Sigma^+$ state are given by

$$\epsilon_{\nu, J} = \nu (\omega_e - \omega_e x_e) - \nu^2 \omega_e x_e + B_e J(J+1) - \alpha_e (\nu + \frac{1}{2}) J(J+1) - [D_e + (\nu + \frac{1}{2}) \beta_e] [J(J+1)]^2 \quad \text{for } \nu \geq 0 \text{ and } J \geq 0. \quad (3.5)$$

The zero of energy is chosen to be $\epsilon_{0,0}$, and the values of the constants as reported by Sulzman²⁵ are listed in Table 3.3. The R branch transition ($\Delta\nu = 1, \Delta J = 1$) from the ν, J state has wave number $\omega_{\nu, J}^R$ which is given by

$$\omega_{\nu, J}^R = \omega_e - 2\omega_e x_e (\nu + 1) + 2(\nu + 1) [B_e - (\nu + \frac{1}{2}) \alpha_e] - \alpha_e [J+1][J+2] - 4[D_e + (\nu + \frac{1}{2}) \beta_e] [J+1]^3 - \beta_e (J+1)^2 (J+2)^2 \quad \text{for } \nu \geq 0, J \geq 0 \quad (3.6)$$

TABLE 3.2

Precise Wave Numbers of CO₂ Lines (From Ref. 24)

P(22)	$\omega = 942.380 \text{ cm}^{-1}$
P(20)	$\omega = 944.190 \text{ cm}^{-1}$
P(18)	$\omega = 945.976 \text{ cm}^{-1}$

TABLE 3.3

Molecular Constants for $\text{AlO X } ^2\Sigma^+$ State
(From Ref. 25)

$$\omega_e = 979.23 \text{ cm}^{-1}$$

$$\omega_e X_e = 6.97 \text{ cm}^{-1}$$

$$B_e = .64136 \text{ cm}^{-1}$$

$$\alpha_e = .0058 \text{ cm}^{-1}$$

$$D_e = 1.08 \times 10^{-6} \text{ cm}^{-1}$$

$$\beta_e = 2 \times 10^{-8} \text{ cm}^{-1}$$

whereas the P branch transition ($\Delta v = 1, \Delta J = -1$) has wave number $\omega_{v,J}^P$ given by

$$\omega_{v,J}^P = \omega_e - 2\omega_e x_e (v+1) - 2J [B_e - (v + \frac{1}{2})\alpha_e] - J(J-1)\alpha_e + 4J^3 [D_e + (v + \frac{1}{2})\beta_e] - J^2 (J+1)^2 \beta_e \quad (3.7)$$

for $v \geq 0$ and $J \geq 1$.

The Q branch transition ($\Delta v = 1, \Delta J = 0$) is not present for a Σ state. In terms of the integrated cross section for a given R branch transition, which we denote by $\frac{e^2 \pi}{mc} f_{v,J}^R$, the integrated absorption coefficient for the transition is

$$\int_{\text{line}} \kappa_L(\omega) d\omega = n_{\text{AlO}} \frac{2e^{-1.43883 \epsilon_{v,J}/T}}{Z_{\text{el},v,J}} \left(\frac{e^2 \pi}{mc} f_{v,J}^P \right) \quad (3.8)$$

where $Z_{\text{el},v,J}$ is the partition function for AlO, including electronic, vibrational, and rotational states, 2 is the electronic degeneracy factor of the ground state $X^2\Sigma^+$, n_{AlO} is the concentration of aluminum oxide molecule, e is the charge of the electron, m is the mass of the electron and c is the velocity of light. An analogous formula holds for the P branch transitions.

The detailed line profile $L(\omega)$ must be used to determine the absorption coefficient at the laser wavenumber. Two mechanisms broaden the molecular rotation lines: (1) Doppler broadening which has a half-half width given by

$$b_D = \left(\frac{2kT \ln 2}{M c^2} \right)^{1/2} \omega_0 = 3.6 \times 10^{-7} \sqrt{\frac{T}{A}} \omega_0 [\text{cm}^{-1}] \quad (3.9)$$

where ω_0 is the wave number of the line, M is the mass of AlO and A is its atomic weight; and (2) collision broadening which has a half-half width b_c . The parameter b_c , for most molecules, is of the order of $.08 \text{ cm}^{-1}$ at 300°K and 1 atmosphere, and it scales roughly as $1/\sqrt{T}$ at constant pressure.²⁶ In the regime considered here, collision broadening is 5 times larger than Doppler broadening, so that the Voigt line profile closely resembles a Lorentz profile²⁷ with an effective half-half width given by

$$b_c = b_D + b_c \quad (3.10)$$

The profile function is then given by

$$L(\omega) = \frac{b/\pi}{b^2 + (\omega - \omega_0)^2} \quad (3.11)$$

The total effective absorption coefficient for a laser line ω_L is determined by summing over the contributions from all lines and by then multiplying by $(1 - e^{-1.43883 \omega_L/T})$ in order to include simulated emission. Applying this procedure to Eq. (3.11) and (3.8) we find

$$\kappa_L' = \left(1 - e^{-1.43883 \omega_L/T}\right) \frac{e^2 \pi}{mc} \frac{2 n_{\text{AlO}}}{Z_{\text{el}, \nu, J}} \sum_{\nu, J} e^{-1.43883 \epsilon_{\nu, J}/T} \quad (3.12)$$

$$\left\{ \frac{f_{\nu, J}^R b_{\nu, J}^R / \pi}{(b_{\nu, J}^R)^2 + (\omega_{\nu, J}^R - \omega_L)^2} + \frac{f_{\nu, J}^P b_{\nu, J}^P / \pi}{(b_{\nu, J}^P)^2 + (\omega_{\nu, J}^P - \omega_L)^2} \right\}$$

where $b_{\nu, J}^R$ and $b_{\nu, J}^P$ are the half-half widths of the R and P transitions respectively, from the ν, J state.

The final ingredients needed are the f numbers of all the transitions. Fortunately the f numbers of different vibrational-rotational transitions are related by simple formulas. The quantum mechanical formula for the f number is

$$f = \frac{8\pi^2 m_e c^2 \omega}{3 h_p e^2} |M_e|^2 \quad (3.13)$$

where M_e is the electric dipole moment of the transition, m_e is the mass of the electron, c is the velocity of light, h_p is Planck's constant, e is the charge of the electron and ω is the wave number of the transition. Only ω and M_e change for different transitions. For a molecular system with the energy levels approximated by an harmonic oscillator, the only transition moment is between adjacent vibrational states, $\Delta v = 1$. Furthermore the strength of the transition moment is proportional to $(v + 1)$. (Hereafter we call this the harmonic scaling law). Finally the relative strength of the two allowed angular momentum transitions are given by the Hönl-London factors: $\frac{J+1}{2J+1}$ for R transitions, $\frac{J}{2J+1}$ for P transitions.

Therefore, if the f number for one transition, say the R transition for $v = 0, J = 0$ is known, the f numbers of all other transitions are given by

$$f_{v,J}^R = \frac{J+1}{2J+1} (v+1) f_{00}^R \frac{\omega_{v,J}}{\omega_{0,0}} \quad (3.14)$$

$$f_{v,J}^P = \frac{J}{2J+1} (v+1) f_{00}^R \frac{\omega_{v,J}}{\omega_{0,0}}$$

The value of f has been theoretically predicted by Michels.²⁸ One model he used predicted $f = 8.58 \times 10^{-6}$ for $v = 0$, and transitions from high v states were found to be close to $(v + 1) f$. Furthermore, $\Delta v \neq 1$ transitions were suppressed. Unfortunately another model led to the value $f = 1.25 \times 10^{-5}$. However, for the most important transitions in our calculations, the transitions from the $v = 5$ state, strong anharmonic effects in the second method of calculation reduce the f number to 5.15×10^{-5} which agrees well the value $6 \times 8.58 \times 10^{-6}$ which is given by the first model and the harmonic scaling law. Therefore, the f number of 8.58×10^{-6} and the harmonic scaling law were used in our calculations. We assumed that the value quoted is correct for the $f_{0,0}$ transition,²⁹ and that Eqs. (3.14) define all the other required f numbers.

Calculations of the absorption by Al_2O_3 vapor for the P(18), P(20) and P(22) lines of CO_2 were performed by using Eqs. (3.12) and (3.14), $f_{0,0} = 8.58 \times 10^{-6}$ and $b_c = .08\sqrt{300/T}$. The results are shown in Fig. 3.7. The dominant laser line, P(20), is seen to be also the most strongly absorbed; hence breakdown most likely occurs when the laser lases on the P(20) line. All subsequent calculations therefore assume the laser fires on the P(20) line. The total absorption coefficient is plotted in Fig. 3.8. It can be seen that molecular absorption in AlO exceeds inverse Bremsstrahlung absorption in the crucial low temperature regime.

The molecular absorption coefficient is very sensitive to two factors - (1) the position of the laser line and (2) the collision broadening of the lines. In our calculations reliable values of the line positions were used, but the collision broadening was only estimated. If the true half width is much larger than the value used here, absorption is enhanced; if it is much smaller, absorption is hindered. More accurate predictions of molecular absorption require reliable values for the collision half widths.

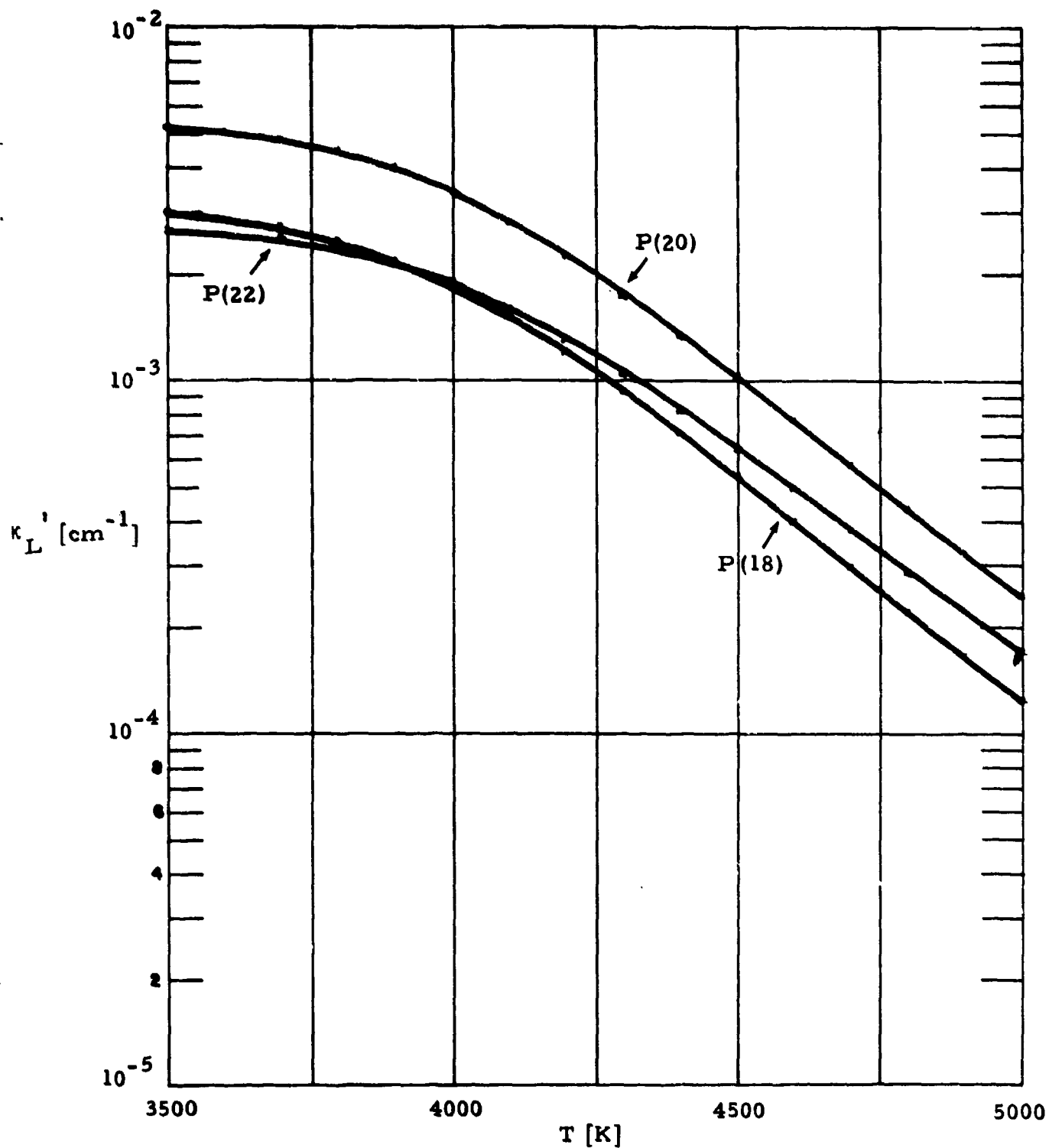


Fig. 3.7 Contribution of Molecular Absorption to Effective Absorption Coefficient of 10.6μ Radiation for Al_2O_3 Vapor in Equilibrium at One Atmosphere. The coefficient is shown for three separate CO_2 laser lines.

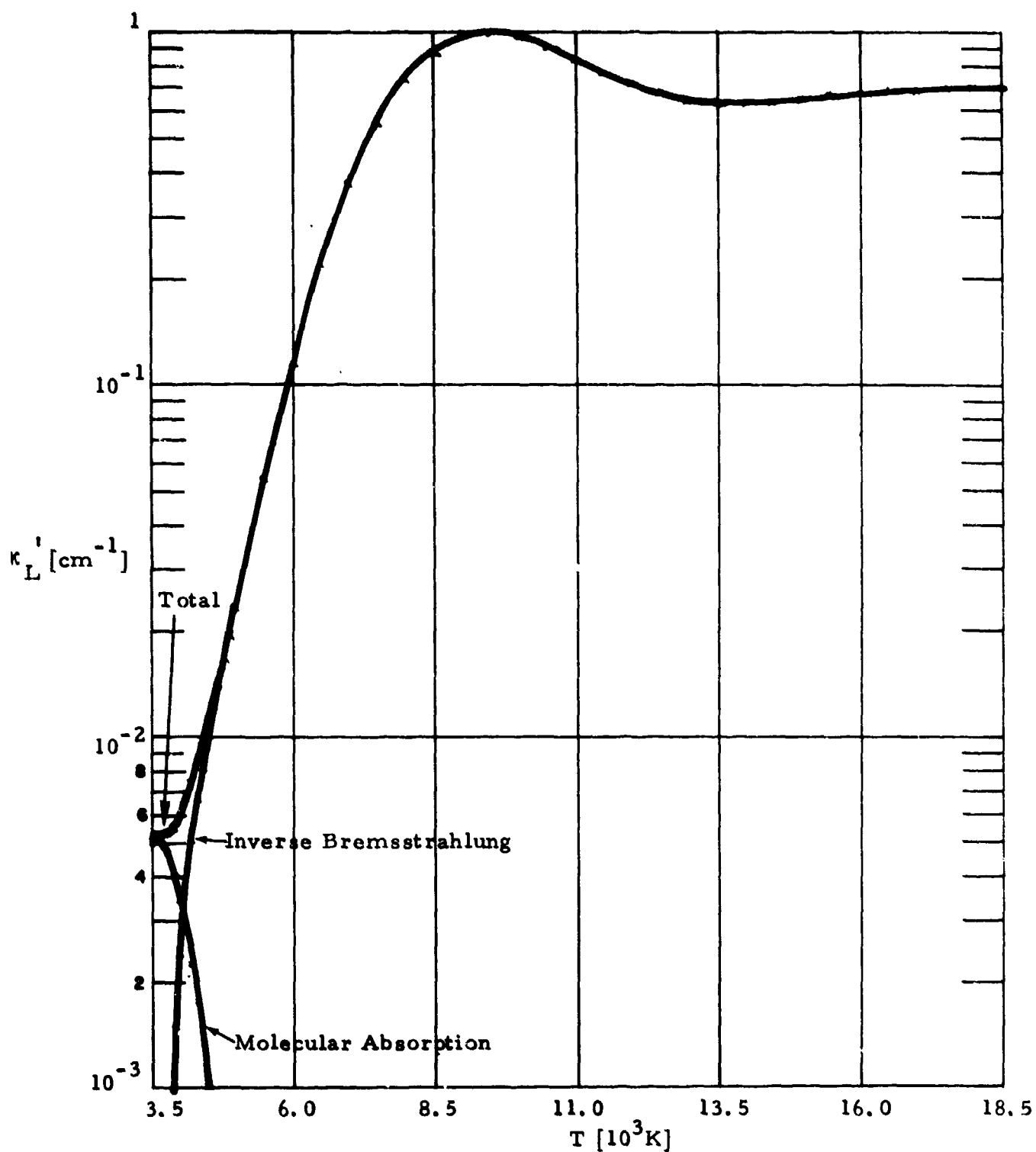


Fig. 3.8 Total Effective Absorption Coefficient for P(20) Laser Line by Al_2O_3 Vapor in Chemical Equilibrium at One Atmosphere Pressure. The molecular absorption contribution and inverse Bremsstrahlung contribution are also plotted.

3.5 Thermal Conduction Losses

The dominant loss at low temperature is thermal conduction of energy from the hot Al_2O_3 vapor into the cold surrounding air. The losses at any given time depend upon the local temperature profile, which itself is determined by the past history of vapor production, laser heating and thermal conduction losses. In this report, however, a simplistic model has been adopted wherein there is no significant heat addition or loss during the production of the vapor cloud, and, once the cloud is formed, it heats without further production of vapor from the particle.

The magnitude of the losses from the vapor cloud due to thermal conduction are estimated by determining the losses from a sphere of radius $R(T)$ which is maintained at a constant temperature T . The losses are therefore characterized by the thermal behavior of the air; that is, by solving the equation

$$(\rho c_p) \frac{dT}{dt} = \frac{1}{r^2} \frac{\partial}{\partial r} \left(r^2 \lambda_c \frac{\partial T}{\partial r} \right) \quad (3.15)$$

in the region $r \geq R$, where ρc_p and λ_c are the density, specific heat, and equilibrium thermal conductivity of air. In making this approximation, it has been assumed that the transport of energy caused by the diffusion of Al_2O_3 vapor into the air and the simultaneous diffusion of air into the Al_2O_3 vapor is well approximated by the self diffusion within air itself. This approximation seems reasonable since the diffusion velocities of all heavy components are expected to be of the same magnitude.

The time dependent solution of Eq. (3.15) for constant λ_c and ρ for initial air temperature T_0 and for vapor temperature T_v is given by³⁰

$$(T - T_o) = (T_v - T_o) \frac{R}{r} \int_{\frac{|r-R|}{2\sqrt{Kt}}}^{\infty} e^{-u^2} du \quad (3.16)$$

where K is the diffusivity $\lambda_c / \rho c_p$. The energy flux at the surface of the vapor cloud is simply

$$-\left. \frac{\lambda \partial T}{\partial r} \right|_{r=R} = \frac{\lambda (T_v - T_o)}{R} \left[1 + \frac{R}{\sqrt{\pi Kt}} \right]. \quad (3.17)$$

For short times the transient term $R/\sqrt{\pi Kt}$ can dominate, but for long times the conduction losses approach a steady state value of $\lambda (T_v - T_o)/R$.

The steady state limit can also be determined for variable $\lambda_c(T)$. The requirement that $\partial T / \partial t$ be zero reduces Eq. (3.15) to

$$r^2 \lambda(T) \frac{dT}{dr} = \text{constant}. \quad (3.18)$$

Invoking the conditions $T(R) = T_v$, and $T(r \rightarrow \infty) = T_o$, we find

$$r \int_{T_o}^{T(r)} \lambda(T) dT = R \int_{T_o}^{T_v} \lambda(T) dT. \quad (3.19)$$

The flux at the surface is then given by

$$-\left. \frac{\lambda dT}{dr} \right|_{r=R} = \frac{\int_{T_o}^{T_v} \lambda(T) dT}{R}. \quad (3.20)$$

The quantity $\int \lambda dT$ for air is plotted in Fig. 3.9. The values of $\lambda(T)$ were taken from Yos³¹ for $T \geq 2000^\circ\text{K}$ and from Ref. 32 for $2000^\circ\text{K} \geq T \geq 300^\circ\text{K}$.

Thermal conduction losses are calculated as surface fluxes. It is necessary, however, to know how those losses are distributed within the volume of the hot vapor cloud. For short times, the losses occur entirely within a small layer of vapor adjacent to the cold air. At long times, a situation is reached wherein the losses are spread uniformly over the vapor volume. Therefore it is important to determine when the losses affect the vapor cloud as a whole, rather than only the outer layers. A crude estimate has been made as follows: The solution for the cooling of a sphere initially at temperature T_v , in the absence of any heat sources, is given in Ref. 33. Inspection of a plot of the solution suggests that the central temperature drops 5% when $\sqrt{Kt/R^2} = .25$. Assuming that thermal conductivity of Al_2O_3 vapor is the same as air, $\lambda_c = 5.85 \times 10^{-3} \text{ W/cm K}$, and using ρc_p of the vapor at 4000°K ($1.3 \times 10^{-3} \text{ J/cm}^3$), we find the time at which the losses affect the whole volume to be $17 \mu\text{sec}$ for the cloud formed by evaporating 65.8% of a Al_2O_3 particle of 15μ radius. This time will be used in subsequent calculations to determine when thermal conduction effects are important.

3.6 Radiation Losses

The radiation losses were computed for a sphere of Al_2O_3 vapor assuming that atomic line radiation, atomic recombination radiation and Bremsstrahlung were the important contributions. This assumption is valid at high temperatures where the radiation losses from the plasma and radiative transfer to the surrounding air are potentially important factors.

The absorption coefficient for inverse Bremsstrahlung was determined from Kramer's formula (Eq. (3.3)) with a constant Gaunt factor of 1.6. The calculation of the absorption coefficient for bound-free transitions included the transitions from all the levels listed by Moore.¹⁶

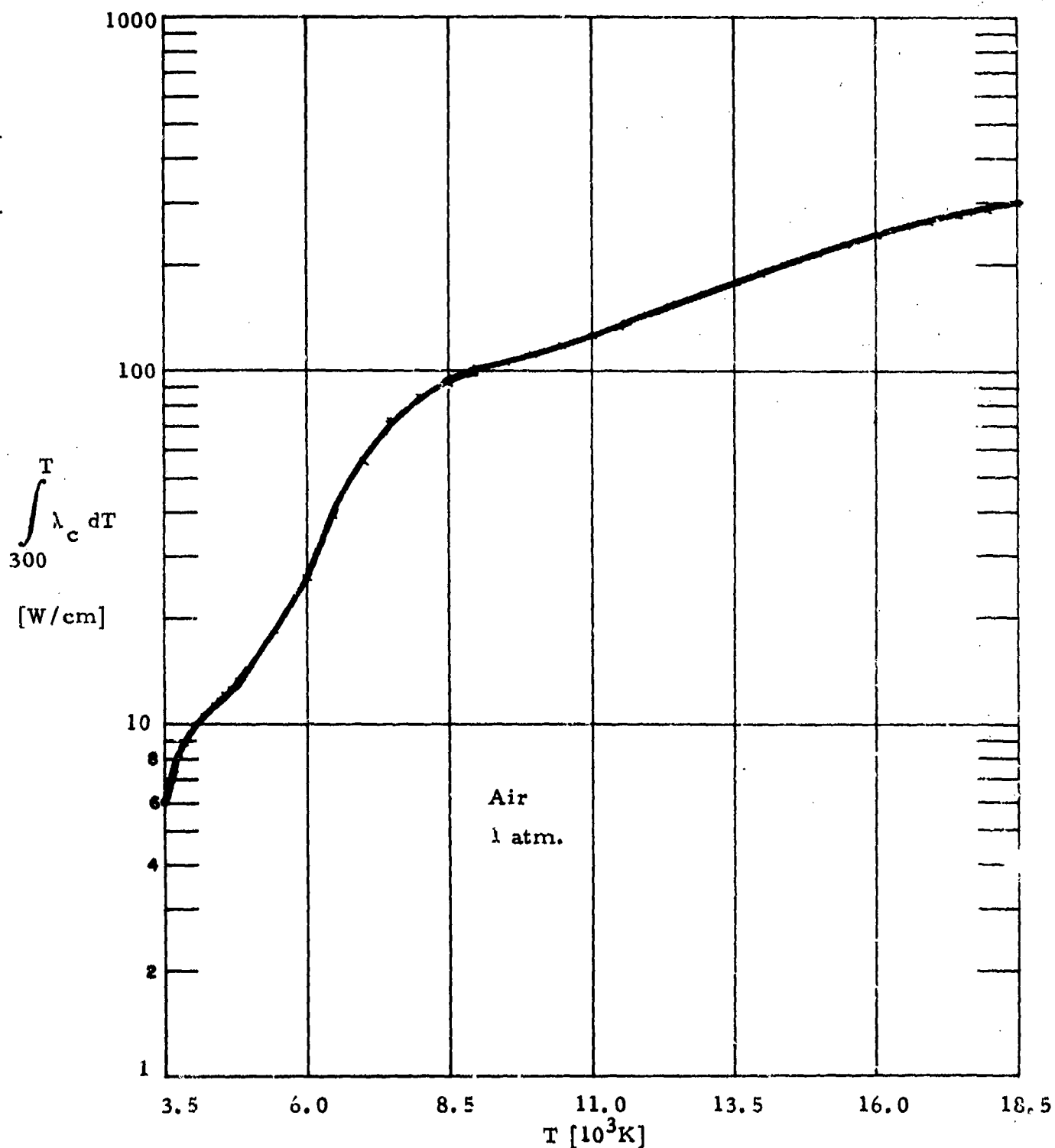


Fig. 3.9 Integral of Equilibrium Thermal Conductivity of Air from 300°K to T. Steady state conduction loss per unit volume from sphere of radius R is given by $3 \int \lambda_c dT / R^2$.

Estimates of the cross section of photoionization of the ground state were taken from an survey of experimental data by Hudson and Kieffer³⁴ for Al and from the theoretical calculation by Thomas and Helliwell³⁵ for O. The cross sections of all higher states were determined by the hydrogenic approximation.³⁶ The inverse Bremsstrahlung absorption coefficient and the photoionization absorption coefficient were added together to yield an effective continuum absorption coefficient. The total surface flux for continuum radiation, including the effects of reabsorption, was then determined for a sphere of uniform temperature T and radius R(T)

The flux attributable to atomic line transitions was calculated for the lines and f numbers listed by the NBS tables for Al⁺, Al³⁷ and O.³⁸ The width was determined by the Stark broadening parameters of Griem.³⁹ The flux from each line was computed without including the effects of other lines or the continuum, but reabsorption by the line itself was properly included. The neglect of Al⁺⁺ and O⁺ atoms, as well as the omission of other broadening mechanisms, can be justified by simple estimates of their contribution to the overall flux in the high temperature region. Stark broadening dominates except at low temperatures where radiation is unimportant. The O⁺ and Al⁺⁺ ions may be plentiful, but their emission occurs in the extreme ultraviolet which is an unimportant region of the radiation spectrum.

The predictions for $\beta = .125$, $.658$ and 1.0 are plotted in Fig. 3.10. The continuum radiation tends to be small and transparent. The dominant losses are from "black" lines. The losses are seen to be very small at low temperatures; however, they increase rapidly and dominate over thermal conduction above 14000°K .

The calculations discussed above are suitable for high temperatures. At low temperatures molecular emission may be significant. Fortunately the only species which radiates in the important region of the spectral range at low temperature is AlO. Furthermore it is the most prevalent molecule.

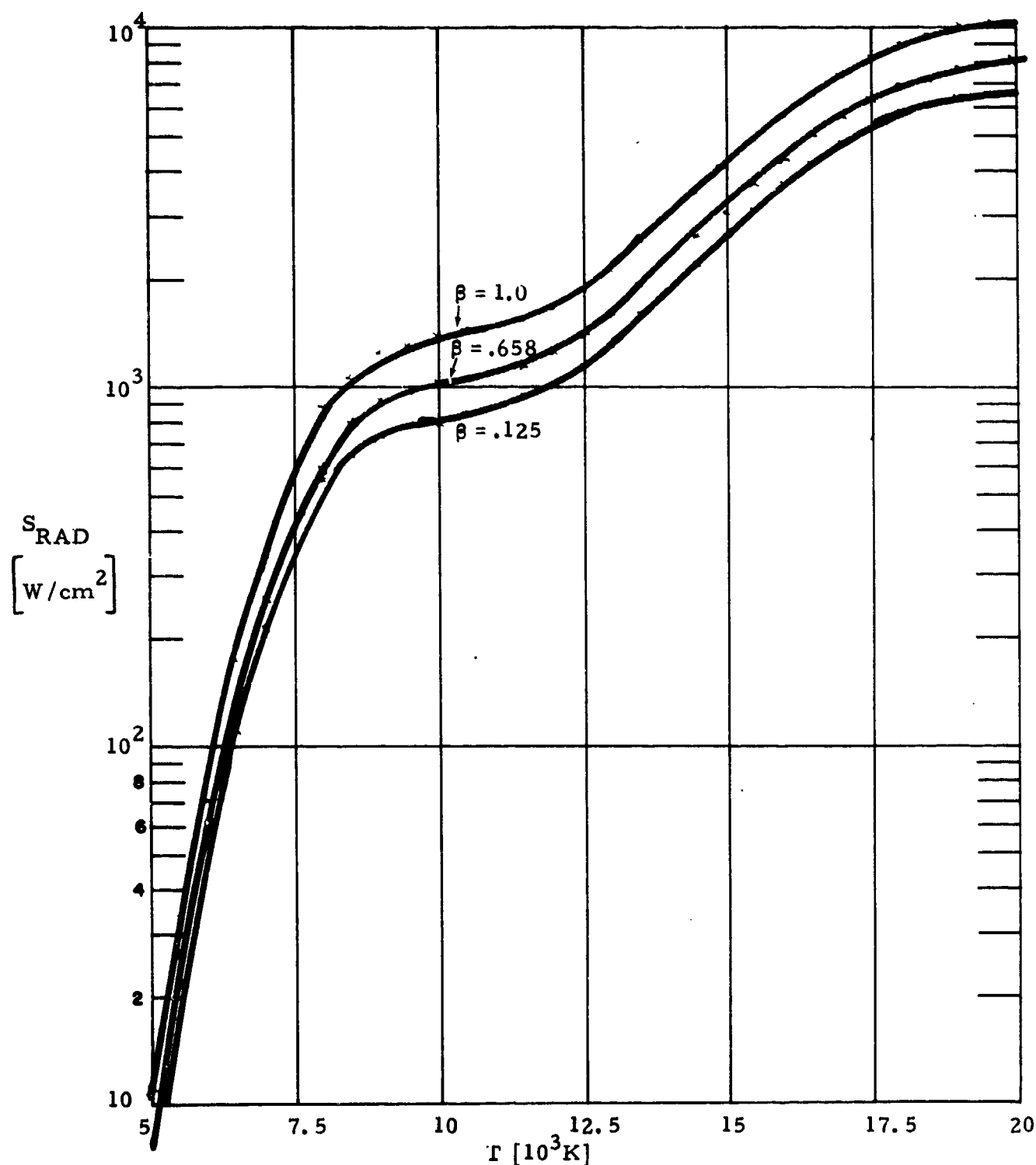


Fig. 3.10 Radiation Flux at Surface of Vapor Cloud Formed by Evaporating a Fraction β of a Al_2O_3 Particulate Which has a Radius of 15μ . Atomic lines transitions and photo recombination are the main contributions.

Therefore the contribution from all molecular emissions is expected to be composed mostly of the transition from the $B^2\Sigma^+$ state to the $X^2\Sigma^+$ state of AlO. The oscillator strength for all transitions ($\Delta v = 0, \pm 1$) is $^{40} 1.12 \times 10^{-2}$. The band occurs near $\omega = 20635 \text{ cm}^{-1}$. Assuming transparent emission, which is the maximum possible emission, we find the radiation loss from molecular radiation to be 210 W/cm^3 at 4000°K . This loss is less than two percent of the absorption rate for $I_o = 3 \times 10^6 \text{ W/cm}^2$, thus molecular emission is unimportant for the determination of heating rates.

3.7 No Loss Approximation

Shortly after vaporization begins, a layer of vapor is produced which protects the vapor subsequently produced from the cooling effect of thermal conduction into the air. In Subsection 3.5 the time for which this protection lasts was crudely estimated to be $17 \mu\text{sec}$ for a 65.8% vaporized particle. Therefore the first few microseconds of vapor heating occur uninfluenced by losses due to thermal conduction. The "no loss" approximation, which is valid at short times, is described by

$$\rho c_p \frac{dT}{dt} = \kappa_L' I_o, \quad (3.21)$$

and the time to heat the vapor to temperature T starting from an initial temperature T_s is found from

$$t_T = \frac{1}{I_o} \int_{T_s}^T \frac{\rho c_p}{\kappa_L'} dT. \quad (3.22)$$

A plot of T versus $I_o t$ for $T_s = 4000^\circ\text{K}$ is given in Fig. 3.11. Since similar plots for different choices of T_s correspond to shifts in the origin of the fluence co-ordinate, negative values of fluence were included. The

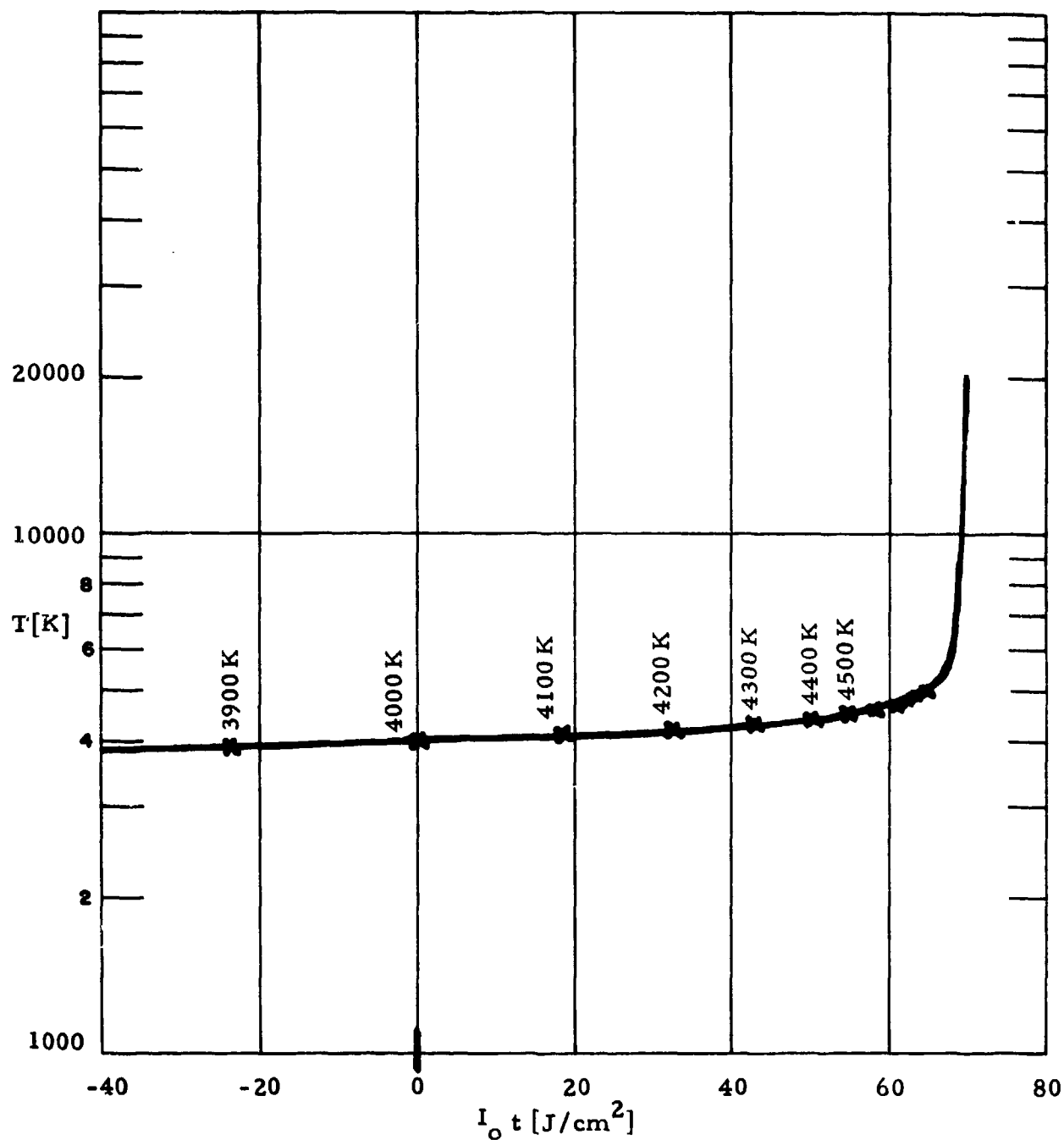


Fig. 3.11 Temperature of Equilibrium Al_2O_3 Vapor as a Function of Fluence - No Loss Approximation. "X" is used to designate each one hundred degree temperature point from 3900 K to 4500 K.

graph dramatically demonstrates that most of the time spent heating the vapor occurs during the initial heating to 5000°K . In the "no loss" approximation, the fluence required to heat the vapor from 4000°K to 20000°K is approximately 71 J/cm^2 . For comparison recall that the fluence necessary to initiate vaporization is 41.4 J/cm^2 while the fluence needed to vaporize a fraction β of the original particle having a 15μ radius is $225 \beta \text{ J/cm}^2$.

If the heating always occurred without losses, the time to vaporize a particle and then to heat the cloud to 20000°K would scale as $I_0 t$. This scaling breaks down at low intensity for two reasons. The first reason, discussed in Section 2, is that a pure vapor cloud cannot be produced. A second reason is that the vapor does not heat sufficiently rapidly to allow losses to be neglected. The time to heat the vapor to 20000°K is very sensitive to the temperature the vapor cloud has achieved when losses become important. Using $17\mu\text{sec}$ as the time over which the "no loss" approximation is valid, we see from Fig. 3.11 that an intensity of $3 \times 10^6 \text{ W/cm}^2$ heats the vapor to 4300°K before losses must be included. If the intensity is $5 \times 10^5 \text{ W/cm}^2$, however, the vapor reaches 20000°K before the $17\mu\text{sec}$ has passed. Thus it is only at the lowest intensities studied here that thermal conduction losses become important.

It should be noted that the model of constant pressure heating in thermodynamic equilibrium does not accurately describe the rapid heating at high temperatures. Even for a flux of $3 \times 10^6 \text{ W/cm}^2$ the model predicts that the vapor heats from 10000°K to 20000°K within $.3\mu\text{seconds}$ - a time of the same magnitude as the time required to equilibrate pressure and maintain chemical equilibrium. However, since the heating rate at high temperature must be slowed down by a factor of ten in order alter the total heating time significantly, the possibility of a non-equilibrium vapor is not pursued here.

3.8 Averaged Loss Approximation

Although the no loss calculations are applicable for strong beams, such as $8 \times 10^6 \text{ W/cm}^2$, as the intensity is lowered, the time to heat the vapor becomes longer than the maximum time over which conduction can be neglected. A simple method of accounting for losses is to average them over the entire volume of the vapor. In earlier subsections $\int \lambda dT$ and S_{RAD} have been determined. The temperature history of the vapor cloud in an averaged loss approximation is described by

$$\rho c_p \frac{dT}{dt} = \kappa_L' I_0 - \frac{3 \int \lambda dT}{R^2} - \frac{3 S_{\text{RAD}}}{R} \quad (3.23)$$

The first calculation to be made in the model is the threshold intensity I_{TH} below which the laser cannot heat the vapor. The right hand side of Eq. (3.23) must be positive for heating to occur, therefore the quantity

$$I_s = \frac{3}{\kappa_L' R} \left(\frac{\int \lambda dT}{R} + S_{\text{RAD}} \right)$$

is the laser intensity which would just sustain the vapor cloud at a given temperature. A plot of I_s permits the threshold intensity for heating of the vapor cloud to be determined by inspection. This quantity is plotted in Fig. 3.12 for three choices of β .

In no heating were to occur without losses being important, the threshold intensity is $1.9 \times 10^6 \text{ W/cm}^2$ for an entirely vaporized particle. The threshold scales as $\beta^{-2/3}$ for partially vaporized particles. Of course it takes infinite time to achieve breakdown at threshold. Experiments limited to a $100 \mu\text{sec}$ pulse length should observe higher thresholds, since the breakdown must occur while the laser is on.

In order to compare the trends predicted in this section with experimental observations, we focus on vapor clouds with $\beta = 65.8\%$ since these are the largest clouds expected to be produced within $100\mu\text{sec}$. From Fig. 3.12 the threshold intensity is predicted to be $4.3 \times 10^6 \text{ W/cm}^2$ if losses are always important. In fact, however, some no loss heating does occur, and the threshold is lowered. At $4 \times 10^6 \text{ W/cm}^2$ we expect no loss heating to occur for $\sim 17\mu\text{sec}$ at which time the typical temperature will be 5000°K . There is then no problem heating the cloud from this temperature to 20000°K , even when losses are included. A more reasonable estimate of the threshold is $3 \times 10^6 \text{ W/cm}^2$. No loss heating raises the temperature to 4300°K . Then the vapor can heat at a rate determined by the averaged loss model. The additional time to heat to temperature T is determined by

$$t_T = \int_{4300}^T \frac{\rho_c c_p dT}{\kappa_L I_0 - 3 \left(\frac{\int \lambda dT}{R} + S_{\text{RAD}} \right) / R} .$$

This number has been calculated for $\beta = 65.8\%$ and $I_0 = 3 \times 10^6 \text{ W/cm}^2$. The primary difference between the no loss time and the averaged loss time occurs during the heating to 5000°K . The heating takes $5\mu\text{sec}$ in the no loss calculation, but it requires $27\mu\text{sec}$ in the averaged loss model. The total time to heat the cloud is $17\mu\text{sec}$ to reach 4300°K , another $27\mu\text{sec}$ to reach 5000°K and $2\mu\text{sec}$ for all subsequent heating. The total time, including the time to produce the vapor, is $60\mu\text{sec}$ if heating of the vapor commences as soon as vaporization begins, but it is $96\mu\text{sec}$ if the heating does not occur until the full 65.8% of the particle is vaporized.

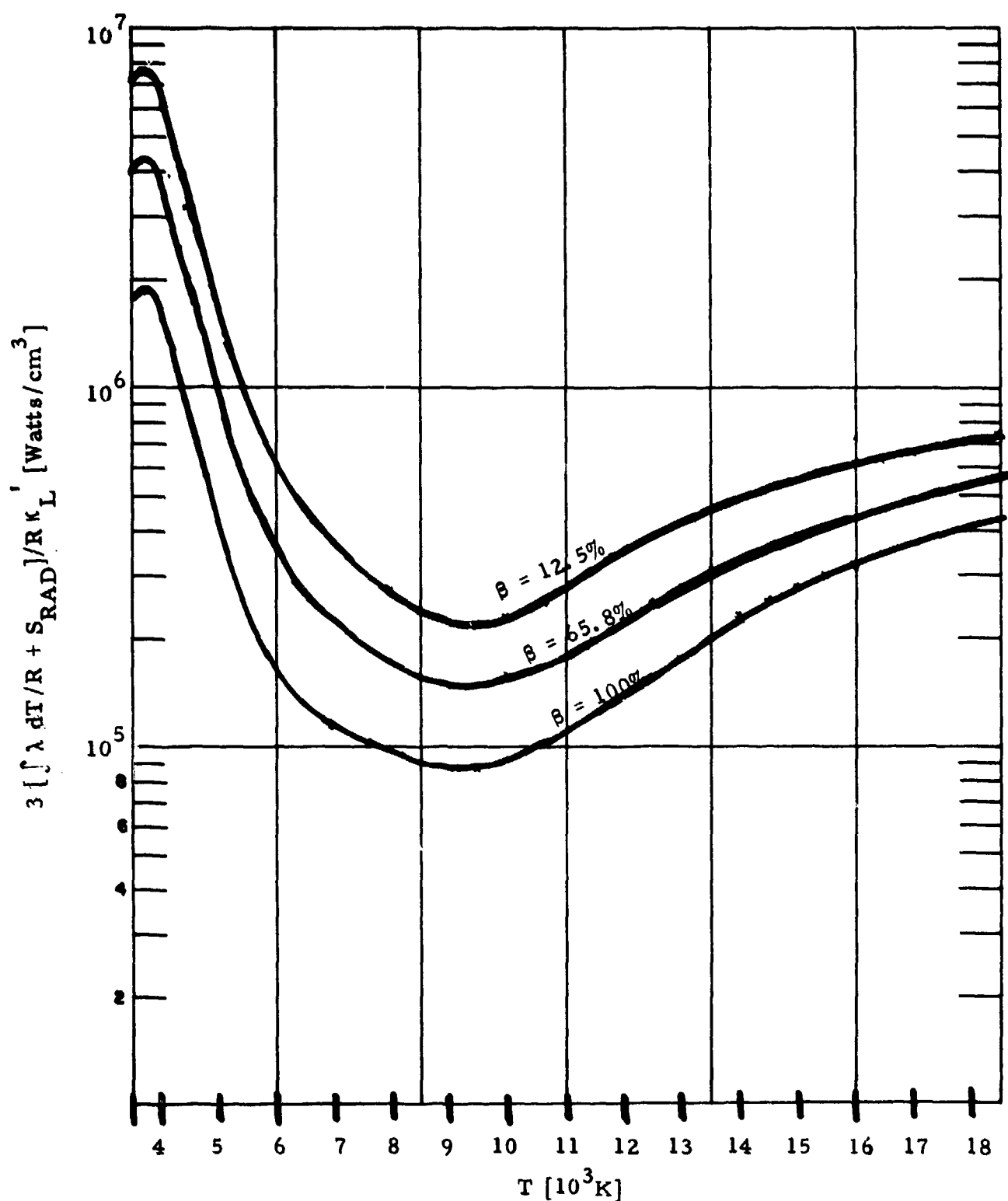


Fig. 3.12 Plot of Laser Intensity Required to Offset Losses for Three Choices of β , the Percent of a 30, μ Diameter Particle which is Vaporized.

In order to demonstrate the importance of losses upon the heating rate, we have plotted in Fig. 3.13 the time rate of change of temperature for two laser intensities. The heating rates for the "no loss" approximation, as well as for the "averaged loss" approximation with $\beta = 1.0$ and $\beta = .658$, are shown. The losses have only a small effect for $I_0 = 8 \times 10^6 \text{ W/cm}^2$, but they are very important for $I_0 = 3 \times 10^6 \text{ W/cm}^2$. Indeed, the temperature at which the transition is made from "no loss" to "averaged loss" is crucial in determining whether or not breakdown occurs for $\beta = .658$ and $I_0 = 3 \times 10^6 \text{ W/cm}^2$.

In summary the models for vapor heating predict that the vapor heats in times consistent with the observed delay times for $I_0 \geq 5 \times 10^6 \text{ W/cm}^2$. The models also predict a threshold near $3 \times 10^6 \text{ W/cm}^2$, but the delay time near the threshold cannot be predicted unambiguously.

If the laser wavelength were changed to 3.8μ , molecular absorption would not be significant and inverse Bremsstrahlung absorption would drop by a factor of ten. The threshold intensity would therefore increase by at least a factor of ten. However, it is possible that other particulates may produce vapors which absorb readily at 3.8μ , and which therefore may heat rapidly at intensities well below the expected threshold for Al_2O_3 . Each particulate and each laser wavelength must be studied individually.

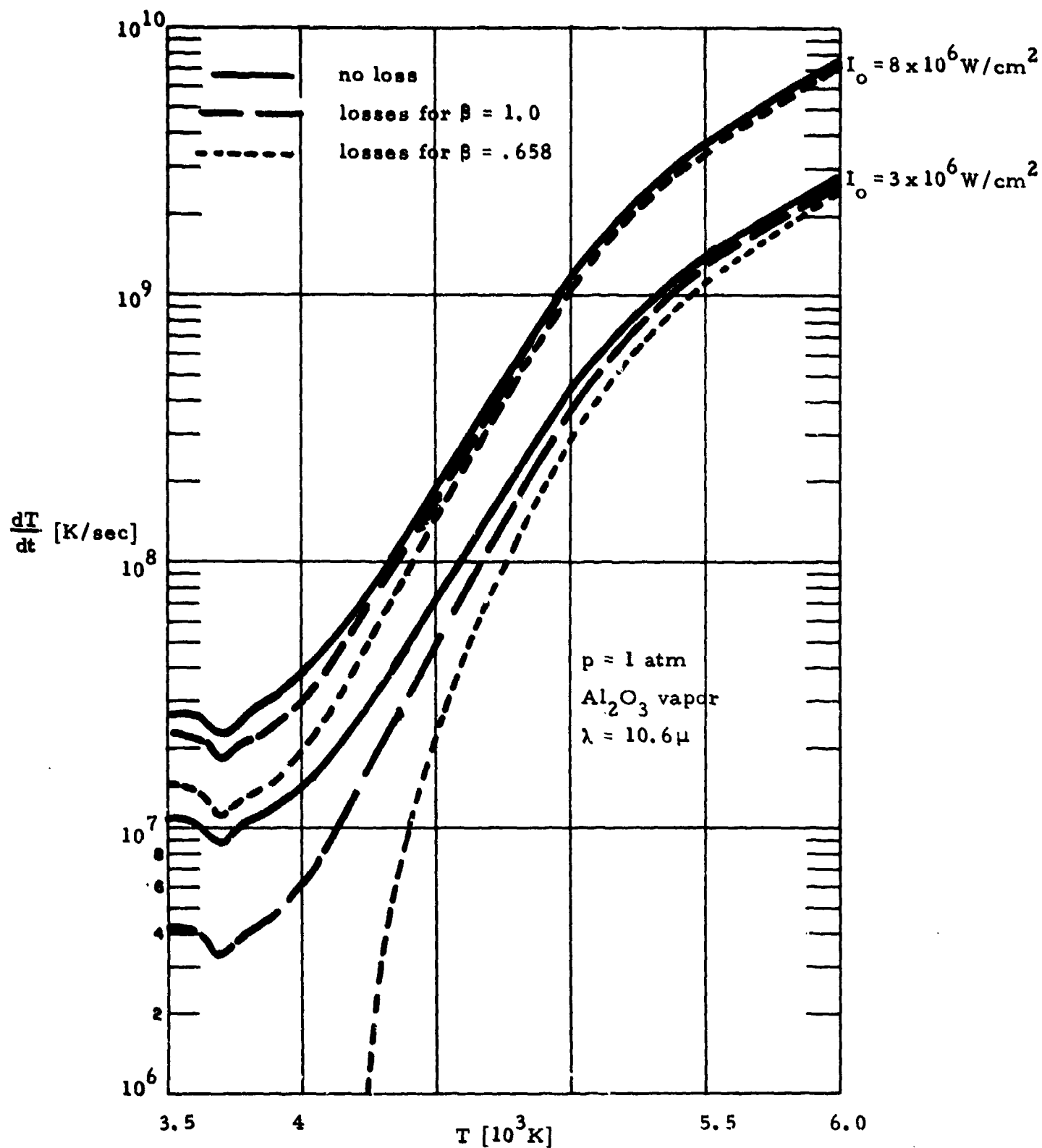


Fig. 3.13 Rate of Change of Temperature with Time, as a Function of Temperature for Equilibrium Al_2O_3 Vapor. Results for three models of losses and two laser intensities are shown.

4. CREATION OF AN AIR PLASMA

A single particulate cannot cause breakdown without first creating an air plasma, since the vapor remains transparent to laser radiation. Recall that at 20000°K the absorption coefficient κ_L is approximately $.6\text{ cm}^{-1}$ and the radius R for an entirely vaporized particle is only $.13\text{ cm}$. Thus the maximum optical depth is $.16$. In this section a simple estimate of the time to create an air plasma is made.

First, the temperature at which the air efficiently absorbs the laser energy must be determined. We adopt the terminology used in laser supported combustion wave models and call this temperature the ignition temperature T_i . For air the only absorption mechanism at 10.6μ is inverse Bremsstrahlung. In Fig. 4.1 a plot of the absorption coefficient of air is compared to the absorption coefficient for Al_2O_3 vapor. The air absorption rate equals the vapor absorption rate at $14,000^{\circ}\text{K}$. When the air reaches the 14000°K , therefore, it is as effective as the vapor in attenuating the laser beam. At intensities of interest, however, the air may heat rapidly at considerably lower temperatures. A plot of $dT/d(t I_0)$ for air is shown in Fig. 4.2. Rapid heating occurs when the rate of change of temperature is $10000^{\circ}\text{K}/\mu\text{sec} = 10^{10}\text{ K/sec}$. For a laser where intensities are near $5 \times 10^6\text{ W/cm}^2$ the value of $dT/d(t I_0)$ should therefore be of the order of $2 \times 10^3\text{ Kcm}^2/\text{J}$. On the basis of the heating rate, the ignition temperature may be as low as 12000°K .

For simplicity we assume that the Al_2O_3 vapor is at 20000°K . It transfers energy to the surrounding air and thereby heats a layer of air to T_i . Once the temperature of the air reaches T_i , it is rapidly heated by the laser to a high temperature - assumed to be 20000°K in the calculations

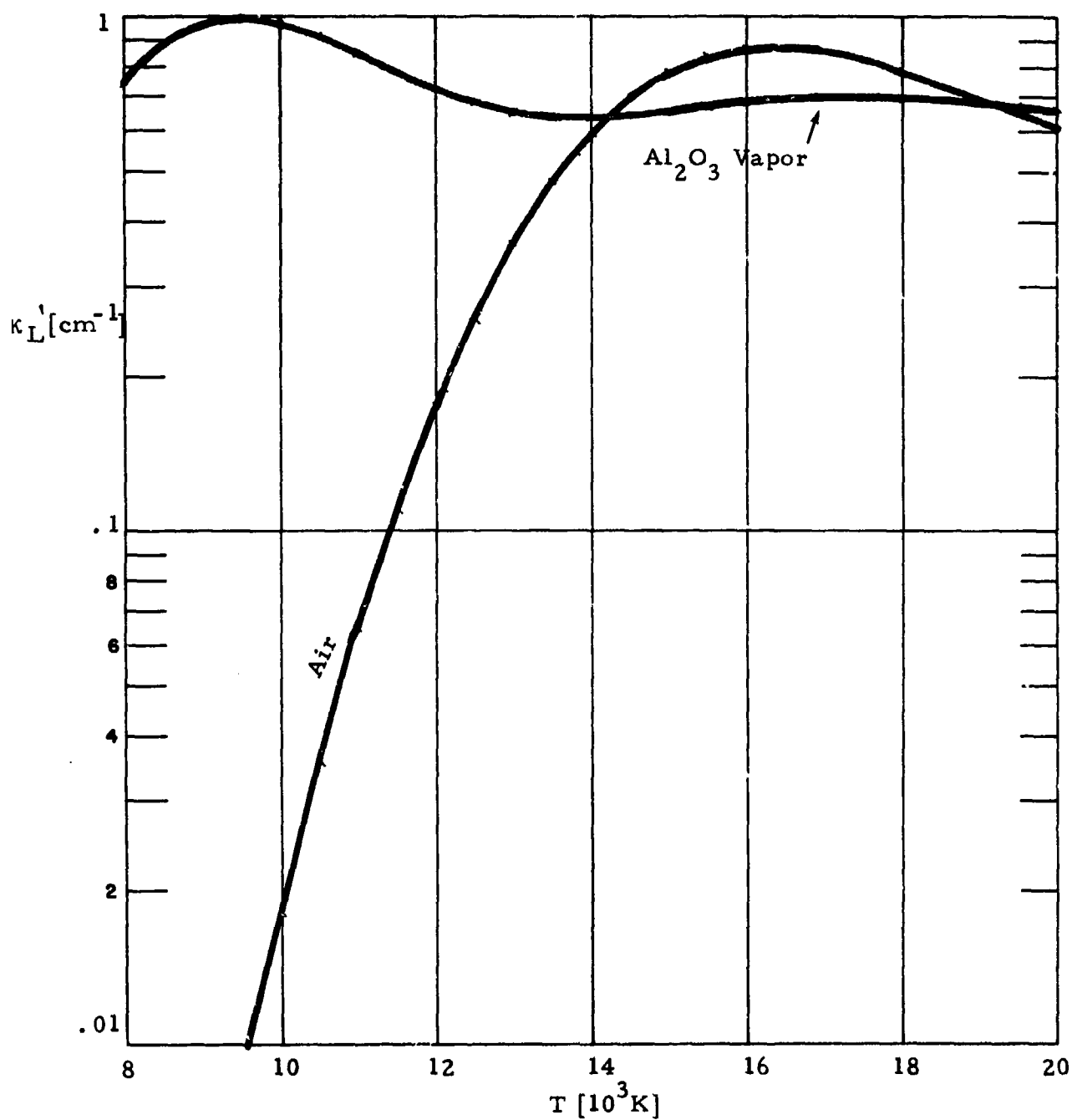


Fig. 4.1 Effective Absorption Coefficient at 10.6μ for Al_2O_3 Equilibrium Vapor and for Air.

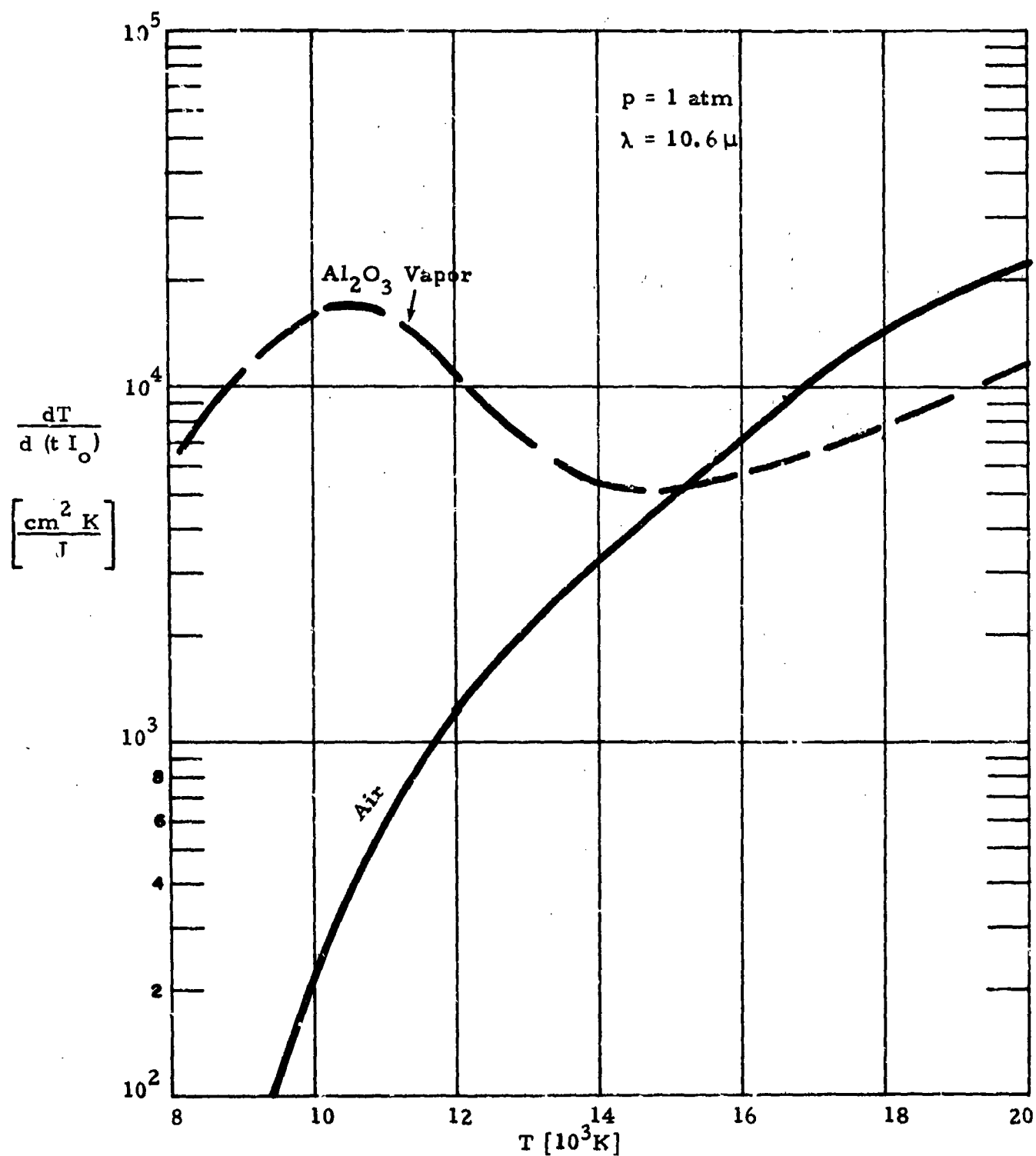


Fig. 4.2 The Rate of Change of Temperature with Fluence as a Function of Temperature for 10.6 μ Radiation.

performed in this section - after which the newly heated air can in turn transfer energy to the surrounding layers of cold air. The rate of expansion of the plasma is given approximately by

$$\rho \Delta h(T_i) \frac{dR}{dt} = q \quad (4.1)$$

where ρ is the density of air at one atmosphere and 20000°K, $\Delta h(T_i)$ is the energy required to heat air from 300°K to T_i and q is the energy flux from the hot plasma. An assumption implicit in Eq. (4.1) is that all the flux q is effective in heating the air in the layer adjacent to the plasma.

The flux q has two components. For small radii, less than .05 cm, thermal conduction is known to be dominant.⁴¹ For large radii the energy flux is controlled by radiation.^{42, 43} Here we are dealing with a transition zone in which both mechanisms contribute. In order to demonstrate that the air is rapidly heated we specialize to a specific example. We choose a particle which is 65.8% vaporized. From Fig. 3.5 the Al_2O_3 vapor cloud is .09 cm in radius at the start of the air heating. The radiative flux in the vacuum ultraviolet (VUV) is approximately 5400 W/cm². Of this radiation only 200 W/cm² lies in the range $h\nu \geq 11$ eV which is the spectral region absorbed by oxygen and nitrogen atoms. The rest of the radiative flux lies in the Schumann-Runge band of molecular oxygen. The flux due to thermal conductivity is given by (see Eq. (3.17))

$$q = \frac{\lambda T}{R} \left(1 + \frac{R}{\sqrt{\pi K t}} \right)$$

which, for air at 20000°K and $t = 10^{-6}$ sec, is 1.5×10^4 W/cm². Therefore the total flux into the air from the hot Al_2O_3 vapor is 2.0×10^4 W/cm². On the other extreme, once the plasma reaches .5 cm in radius, the radiative flux in the region $h\nu \geq 11$ eV is enhanced and becomes nearly

$3.8 \times 10^4 \text{ W/cm}^2$ so that the total radiation is $4.3 \times 10^4 \text{ W/cm}^2$. The flux due to thermal conduction is small because of the preheating caused by radiation. As a first approximation, therefore, a value of $q = 2.0 \times 10^4 \text{ W/cm}^2$ is used to characterize the full regime of interest. This leads to a slight overestimate of the time necessary to produce large plasmas.

The velocity of the plasma front can now be estimated. For T_i of 14000°K , we find $dR/dt = 5 \times 10^4 \text{ cm/sec}$, and for T_i of 12000°K , dR/dt increases to $7 \times 10^4 \text{ cm/sec}$. At either rate the plasma doubles in radius in less than two microseconds. If these estimates of expansion remain accurate for radii as large as .5 cm, it takes a maximum of 8 microseconds to produce a plasma 1 cm in diameter (and perhaps the time is as low as $6 \mu\text{sec}$). The purpose of these calculations is to demonstrate that the air plasma forms very rapidly after the vapor reaches high temperatures. The details of the growth of an air plasma are discussed in the next section.

The effect of laser wavelength and particle composition upon this stage of the breakdown process is uncertain. The air heats at a slower rate if the wavelength is shortened. However, at the intensities considered here, the heating is still rapid. Since the laser is not directly responsible for the heating of the cold air, the most important parameters are the temperature and size of the plasma core, not the laser intensity. Of course the temperature of the core is related to the laser intensity, but for the intensities required to initiate vapor heating the core temperature of the resultant plasma is expected to exceed $20,000^\circ\text{K}$. In short, changes of wavelength and particle composition are not expected to alter the estimates of this section.

5. AIR PLASMA DYNAMICS

The previous sections have dealt with the absorption of laser energy by solid particles, which are either completely or partially vaporized, and the transfer of the energy from the vapor to the surrounding air. The hot air is ultimately heated via inverse Bremsstrahlung absorption until the expanding air plasma becomes opaque to the laser radiation. This plasma propagation mechanism is similar to that of the laser-supported combustion (LSC) wave propagation. For a given particulate distribution, it is difficult to estimate the corresponding initial air plasma bubble distribution for a given pulse time and laser intensity because the particulates may not be completely vaporized. Hence, in this section, we will examine the air plasma growth dynamics with the initial size assumed to be given. For simplicity, we will also ignore the presence of particle vapor which may be important in some cases.

Initial Conditions

The late-time air plasma growth begins when sufficient energy has been transferred from the vapor to the surrounding air such that the high temperature air plasma begins to absorb the laser energy directly. The initial size of the air plasma depends obviously on the size of the vapor which, in turn, depends on the original particulate size, the fraction of solid that vaporizes and the laser intensity.

As mentioned before, the particulates of interest are primarily Al_2O_3 , SiO_2 , and graphite. Now, consider the diameter of the solid particulates to be 10 - 20 μm and the pressure to be 1 atm. Assuming that the solid particulates vaporizes at 1 atm and vaporization temperature T_v and that the equilibrium composition prevails at T_v , one obtains the vapor size (for complete vaporization) to be several hundred μm , Table 5.1.

Table 5.1

Particulates	T_v , K	Components at T_v	Vapor Diameter, μm
Al_2O_3	3200	O, Al, AlO	300 - 600
SiO_2	2500	SiO, O_2	230 - 460
Graphite	5100	C	420 - 840

The particulates may not be completely vaporized and the vapor diameters would then be less than the above values. Assuming complete vaporization, we arbitrarily take the initial air plasma size to be twice the average vapor, i. e., the initial radius $R_i = 0.05$ cm. As will be shown later, the initial radius will be parameterized. Finally from the effective laser absorption coefficient for 10.6μ radiation in air at 1 atm,⁴³ one finds that the absorption coefficient rises from $2 \times 10^{-2} \text{ cm}^{-1}$ at 10,000 K to approximately 0.8 cm^{-1} at 15000 K. For simplicity, we choose the initial temperature, $T_i = 14,000$, which can also be parameterized to assess the effects of T_i on the final solution.

Laser Absorption and Plasma Emission

The phenomenology of air plasma growth involves coupled fluid dynamics and radiant energy transfer. As the air plasma grows, the energy transfer mechanism, which is analogous to that of laser supported combustion (LSC) waves, is dominated by radiation. Since radiation is expected to control the maximum temperature and the expansion velocity of the air plasma, it is important to properly characterize the radiative transport. The local radiative properties are determined by the effective absorption coefficient for inverse Bremsstrahlung⁴³

$$K_v = g \left\{ \frac{16\pi^2}{3} \left(\frac{2\pi}{3m_e k} \right)^{1/2} \frac{h^2 e^6}{c m_e} \right\} \frac{(1 - e^{-\omega/kT}) n_e [n_+ + 4n_{++}]}{(\omega_L)^3 T^{1/2}} \quad (5.1)$$

and

$$g = 0.55 \ln 27 \left(\frac{T}{10^4} \right)^{4/3} (p X_e)^{-1/3}$$

where k is Boltzmann's constant; \hbar is Planck's constant; c is the speed of light; m_e is the electron mass; ω_L is the laser photon energy; T is the temperature; p is the pressure; X_e is the mole fraction of electron; and n_e , n_+ , n_{++} are the number densities of electrons, ions and double ions respectively. Pirri et al,⁴³ have shown that the effective absorption coefficient at 1 atm is approximately 0.8 for temperatures greater than 14000 K (cf Fig. 5.1). The initial diameter of the air plasma is of the order of 0.1 cm or less. Hence the source term in the energy equation can be assumed to be volumetric absorption i. e., $K_\nu I$ where I is the laser intensity.

For the radiative emission from the hot air plasma, Pirri et al,⁴³ have shown that it can be divided into the transparent ($\omega < 11$ eV) and the black ($\omega > 11$ eV) contributions. The transparent band can be written as

$$E_T = 6.3 \times 10^{-10} T n_o \left\{ \frac{kT}{I_{air}} \frac{q_+}{q_o} + 4.2 \right\} e^{-I_{air}/kT} \quad (5.2)$$

where n_o is the number density of neutrals; I_{air} is the ionization potential for air and q_+/q_o is the ratio of the partition functions of ions to neutrals. The UV band ($\omega > 11$ eV), which accounts for most of the axial transport is essentially black, and given by

$$E_B = \int_{11 \text{ eV}}^{\infty} B_\nu d\nu = \frac{2(kT)^4}{h^3 c^2} \int_{11 \text{ eV}}^{\infty} \frac{\bar{\omega}^3}{e^{\bar{\omega}} - 1} d\bar{\omega} \quad (5.3)$$

where

$$\bar{\omega} = \frac{\omega}{kT}$$

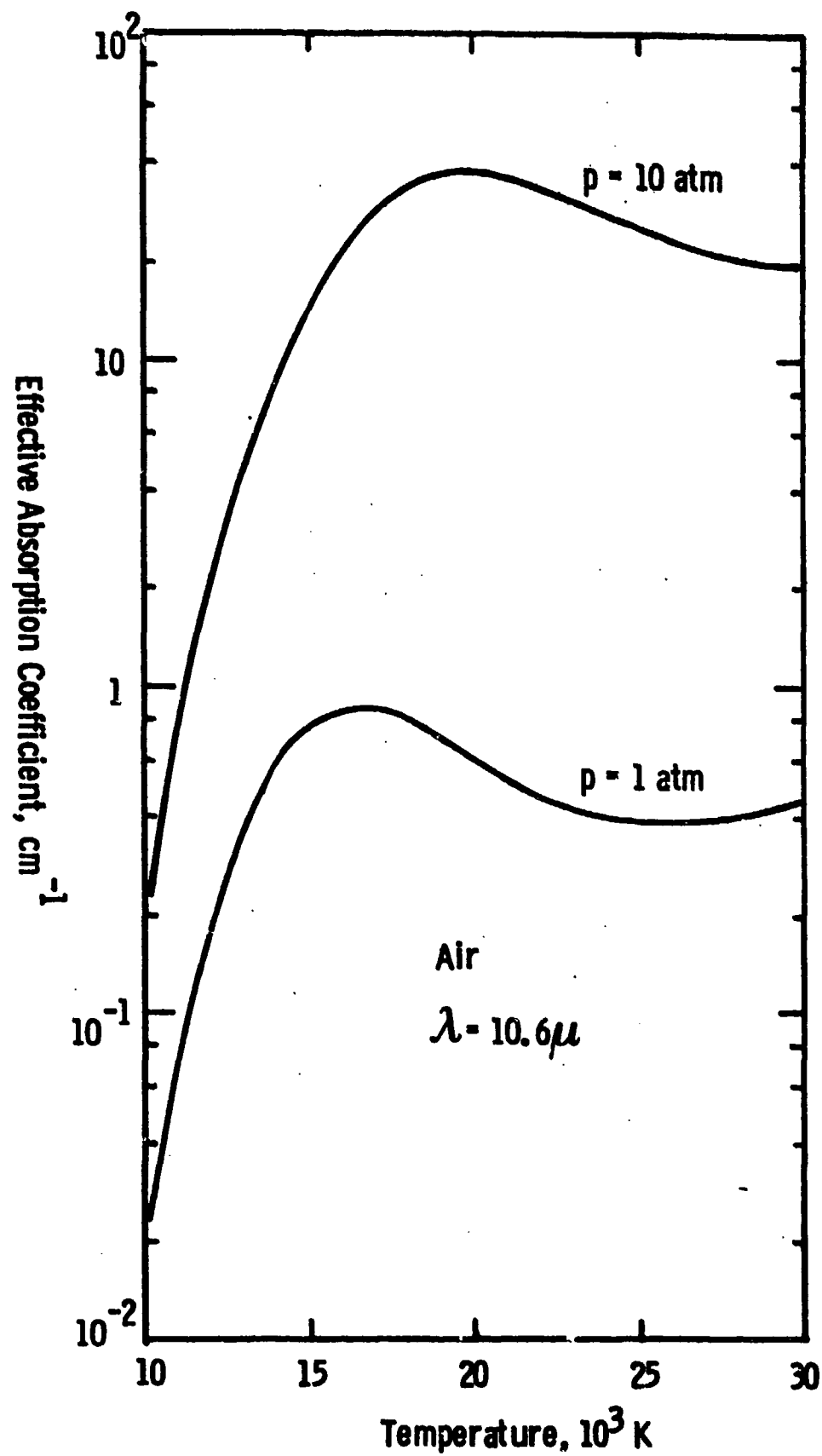


Fig. 5.1 Effective Absorption Coefficient of Air for $\lambda = 10.6 \mu$.

B_ν is the blackbody function and ν is the frequency. For the present calculations, we find that the contribution from the transparent band is negligibly small compared with the UV band and hence the plasma emission in the following analysis will be represented by the UV band alone. With the radiative transport model adapted as above, we can now proceed to examine the air plasma dynamics by means of a perturbation analysis.

Perturbation Analysis

Consider a spherical air plasma of radius R . The governing equation for the growth dynamics can be written as

$$\frac{\partial \rho}{\partial t} + \frac{\partial (\rho u)}{\partial r} + \frac{2 \rho u}{r} = 0 \quad (5.4)$$

$$\frac{\partial u}{\partial t} + u \frac{\partial u}{\partial r} = - \frac{1}{\rho} \frac{\partial p}{\partial r} \quad (5.5)$$

$$\rho \frac{\partial s}{\partial t} + \rho u \frac{\partial s}{\partial r} = \frac{K_\nu I}{T} - \frac{3\pi}{TR} \left(1 + \frac{\Delta h}{\Delta h_a} \right) \int B_\nu d\nu \quad (5.6)$$

$$p = (\gamma - 1) \rho^\gamma \exp \left(\frac{s - s_0}{C_v} \right) \quad (5.7)$$

$$K_\nu = c \frac{\rho^2}{T^{3/2}} \quad (5.8)$$

$$\frac{dR}{dt} = \frac{2\pi k \nu^3 T}{\Delta h_a \rho_a c^2} e^{-h\nu/kT} \quad (5.9)$$

where ρ is the density; u is the radial velocity; S is the entropy; γ is the ratio of specific heats; C_v is the heat capacity at constant volume; Δh_a is the enthalpy difference between the hot air at the edge of air plasma and the cold ambient air; the subscript a indicates ambient condition; and t and r are time and radial distance respectively. Equation (5.9) is derived by equating the UV band emission to the energy consumed by the ingestion of cold ambient air which is then brought to the air plasma temperature.

The above Eqs. (5.4) - (5.9) can be normalized by the following characteristic quantities; the initial sound speed, $a = \sqrt{\gamma R T_i}$, the initial air plasma radius, R_i and a heating time, τ . Then the nondimensional variables are

$$\bar{\rho} = \frac{\rho}{\rho_i}; \quad \bar{u} = \frac{u}{a}; \quad \bar{t} = \frac{t}{\tau}; \quad \bar{p} = \frac{p}{\rho_i a^2}; \quad \dots$$

and the conservation equations become

$$\left\{ \begin{array}{l} \frac{\partial \bar{\rho}}{\partial \bar{t}} + \beta \left[\frac{\partial (\bar{\rho} \bar{u})}{\partial \bar{r}} + \frac{2 \bar{\rho} \bar{u}}{\bar{r}} \right] = 0 \end{array} \right. \quad (5.10)$$

$$\left\{ \begin{array}{l} \frac{\partial \bar{u}}{\partial \bar{t}} + \beta \left[\bar{u} \frac{\partial \bar{u}}{\partial \bar{r}} + \frac{1}{\bar{\rho}} \frac{\partial \bar{p}}{\partial \bar{r}} \right] = 0 \end{array} \right. \quad (5.11)$$

$$\left\{ \begin{array}{l} \bar{\rho} \bar{T} \frac{\partial \bar{s}}{\partial \bar{t}} + \beta \bar{\rho} \bar{T} \bar{u} \frac{\partial \bar{s}}{\partial \bar{r}} = \alpha \bar{K}_v - \left(1 + \frac{\Delta h}{\Delta h_a} \right) \frac{6 \pi \nu^3 k T_i}{I C^2} \frac{T}{\bar{R}} \alpha e^{-\omega_i / \bar{T}} \end{array} \right. \quad (5.12)$$

$$\left\{ \begin{array}{l} \frac{\partial \bar{R}}{\partial \bar{t}} = \frac{2 \pi \nu^3 k \rho_i C_v T_i^2}{\Delta h_a \rho_a C^2 I} \frac{1}{\bar{T}} e^{-\omega_i / \bar{T}} \end{array} \right. \quad (5.13)$$

The characteristic heating time τ has been defined as $\tau = \rho_i C_v T_i R_i / I$. Two basic parameters appear in these normalized equations, the Bouguer Number, $\alpha = K_{v_i} R_i$ which is the ratio of the air plasma radius to the absorption length at the laser frequency, and the Boltzmann Number, $\beta = \rho_i C_v T_i a / I$, which is the ratio of the convective energy flux to the incident radiation energy flux.

For the laser intensity of $10^6 - 10^7 \text{ W/cm}^2$, the initial temperature of 14000 K and the initial pressure of 1 atm, the Boltzmann Number becomes much less than unity. If each of the dependent variables in the nondimensionalized equations is expanded in a series of functions whose coefficients are powers of β , i. e.,

$$\bar{\rho} = \rho_0 + \beta \rho_1 + \beta^2 \rho_2 + \dots$$

the equations can be reduced to sets of equations which appear as coefficients of β . The zero-order solution of the nondimensional momentum equation provides

$$u_0 = 0$$

which indicates that there is no flow and that the growth of the air plasma is by LSC wave mechanism alone. As a result, the problem is reduced to a solution of the energy equation and the LSC wave propagation equation.

$$\left\{ \begin{aligned} \frac{\partial T_0}{\partial t} &= \alpha T_0^{-3/2} - \left(1 + \frac{\Delta h}{\Delta h_a}\right) \frac{6\pi v^3 k T_i}{I C^2} \frac{T_0}{R_0} e^{-\omega_i/\bar{T}_0} \\ \frac{\partial R_0}{\partial t} &= \frac{2\pi v^3 k \rho_i C_v T_i^2}{\Delta h_a \rho_a C^2 I} T_0 e^{-\omega_i/T_0} \end{aligned} \right. \quad (5.14)$$

$$\left\{ \begin{aligned} \frac{\partial R_0}{\partial t} &= \frac{2\pi v^3 k \rho_i C_v T_i^2}{\Delta h_a \rho_a C^2 I} T_0 e^{-\omega_i/T_0} \end{aligned} \right. \quad (5.15)$$

Equations (5.14) and (5.15) have been solved numerically for $T_i = 14,000$ K, $P_i = 1$ atm, $R_i = .05$ cm and laser intensity of 10^6 , 5×10^6 and 10^7 W/cm². With the LSC mechanism alone, the temperature typically climbs from T_i to an almost plateau temperature in less than one μ second. An example temperature profile for $I_0 = 5 \times 10^6$ W/cm² is shown in Fig. 5.2. The air plasma growth, on the other hand, is minimal as shown in Fig. 5.3. For a 100 μ sec pulse, the final plasma radii at the end of the pulse are only 0.057, 0.072 and 0.085 cm for laser intensities of 10^6 , 5×10^6 and 10^7 W/cm² respectively. However, as the intensity increases, the average pressure inside the air plasma increases rapidly. For example, at 10^7 W/cm² it is estimated that the average over-pressure reaches 100 atm at an early time. At the same time, the characteristic time for pressure equilibration at 14,000 K is estimated to be 0.3 μ sec which is short compared with the pulse time of interest, i. e., 100 μ sec. Hence, the air plasma growth becomes dominated by the hydrodynamic effects. In the following section, we will develop a model which will

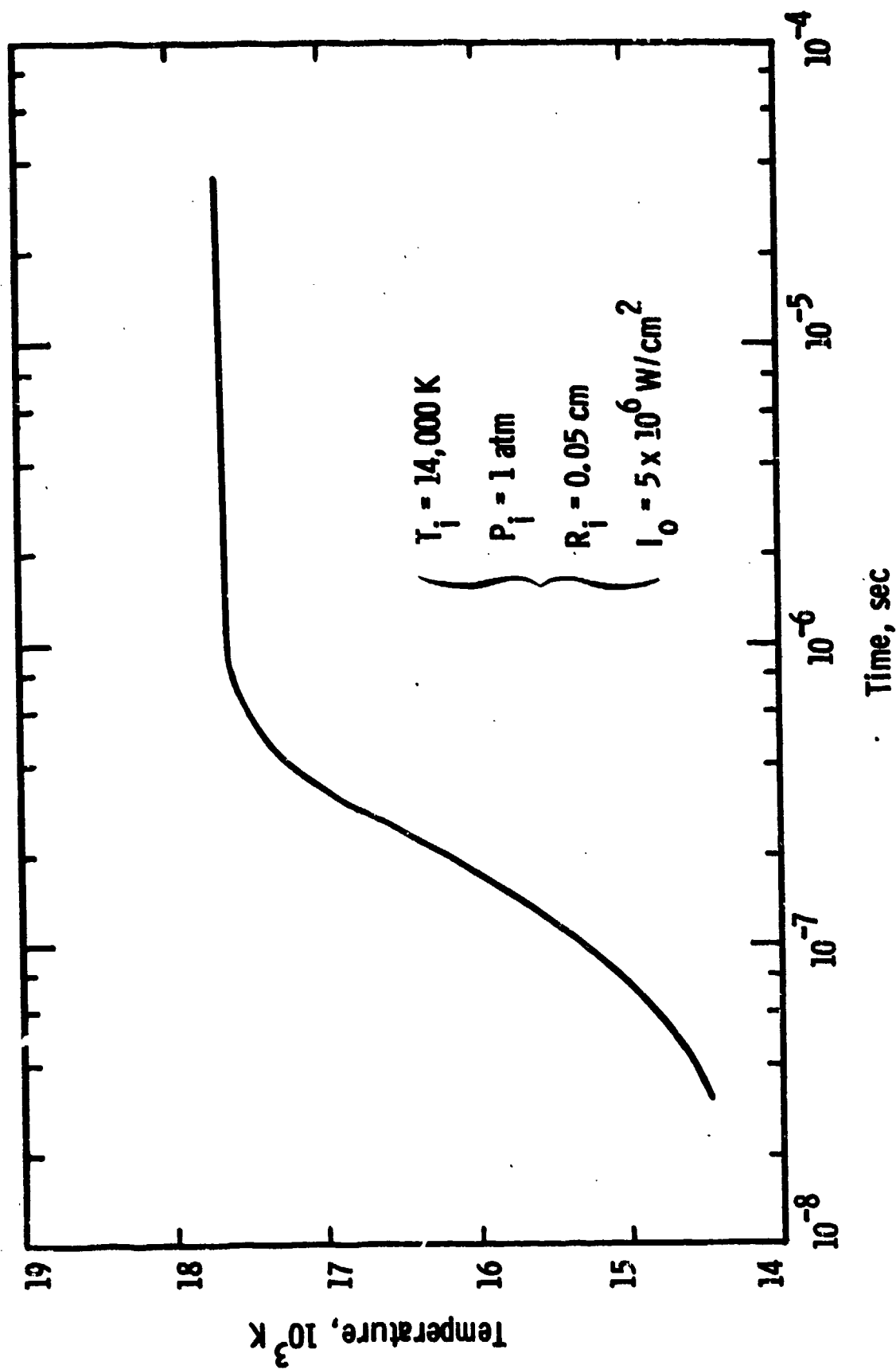


Fig. 5.2 Temperature History of An Air Plasma (LSC Wave Model).

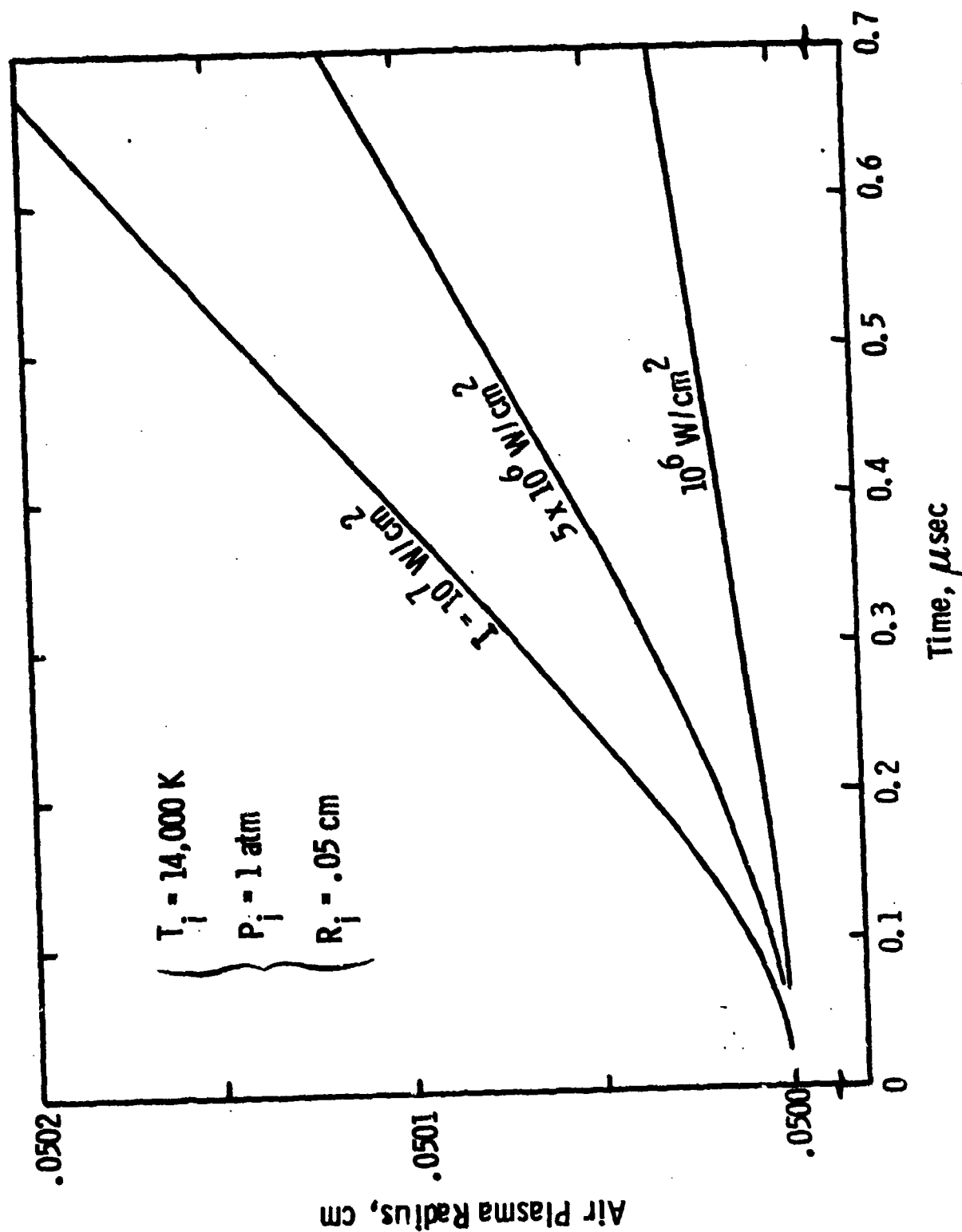


Fig. 5.3 The Air Plasma Growths as Function of Laser Intensity (LSC Wave Model)

incorporate both the ingestion of mass by the LSC wave mechanism and the hydrodynamic expansion as a result of the ingestion.

The "Snow Plow" Analysis

Consider a spherical air plasma which absorbs laser energy. The heated zone propagates outward with the same radiative transfer mechanism as the LSC wave. This outward propagation ingests high density ambient air. As a result of the mass ingestion, the average pressure rises. Here it is assumed that the pressure is instantaneously equilibrated and hence the density and the temperature are uniform inside the air plasma. This high pressure air plasma is then allowed to expand and "push" away the ambient air in a manner similar to that of the "snow plow". For simplicity, the velocity profile inside the air plasma is assumed to be always a linear profile, i. e., $u = u_R(t) r/R$ where u_R is the radial velocity at the air plasma edge.

From the conservation of mass, one gets

$$\frac{d\rho}{dt} = \frac{3\rho_a}{R} \frac{dR_{LSC}}{dt} - \frac{3\rho}{R} \frac{dR}{dt}$$

The first term on the RHS represents the increase of density due to the ingestion of mass while the second term indicates the decrease of density due to the air plasma expansion. Here the expansion equation includes the flow velocity and the LSC wave contribution.

$$\frac{dR}{dt} = u_R + \frac{dR_{LSC}}{dt} = u_R + \frac{E_B}{\rho_a \Delta h_a} \quad (5.16)$$

Hence continuity becomes

$$\frac{d\rho}{dt} = \frac{3}{R} \left[1 - \frac{\rho}{\rho_a} \right] \frac{E_B}{\Delta h_a} - \frac{3\rho}{R} u_R \quad (5.17)$$

From the momentum equation

$$\frac{\partial \vec{u}}{\partial t} + \vec{u} \cdot \nabla \vec{u} = -\frac{1}{\rho} \nabla p$$

one can integrate over the complete volume of the air plasma. Remembering $\rho = \rho(t)$ and Gauss's theorem, we obtain

$$\int_0^{R(t)} \frac{\partial u}{\partial t} 4\pi r^2 dr + \frac{1}{2} \int_0^{R(t)} \frac{\partial u^2}{\partial r} 4\pi r^2 dr = \frac{(p - p_a)}{\rho} 4\pi R^2$$

With the linear velocity profile assumption, the momentum equation can finally be written as

$$\frac{\partial u_R}{\partial t} = \frac{4(p - p_a)}{R\rho} + \frac{u_R E_B}{R\rho_a \Delta h_a}$$

For the energy equation, one has

$$\frac{\partial}{\partial t} \left[\rho \epsilon + \frac{\rho u^2}{2} \right] = - \nabla \cdot \left\{ \rho \vec{u} \left(\epsilon + \frac{p}{\rho} + \frac{u^2}{2} \right) \right\} + Q$$

where ϵ is the internal energy and Q represents the radiative transport (the laser absorption and the plasma emission). Again, we average the entire energy equation over the air plasma volume by integrating. Using the continuity, momentum and the expansion equations, one gets

$$\begin{aligned} \frac{\partial \epsilon}{\partial t} = & \frac{3 u_R}{5 \rho R} (4 p_a - 9 p) + E_a - \left(1 + \frac{\Delta h}{\Delta h_a} \right) \frac{3 E_B}{R \rho} \\ & - \frac{E_B}{R \rho \Delta h_a} \left(1 - \frac{\rho}{\rho_a} \right) \left(3 \epsilon + \frac{9}{10} u_R^2 \right) \end{aligned} \quad (5.19)$$

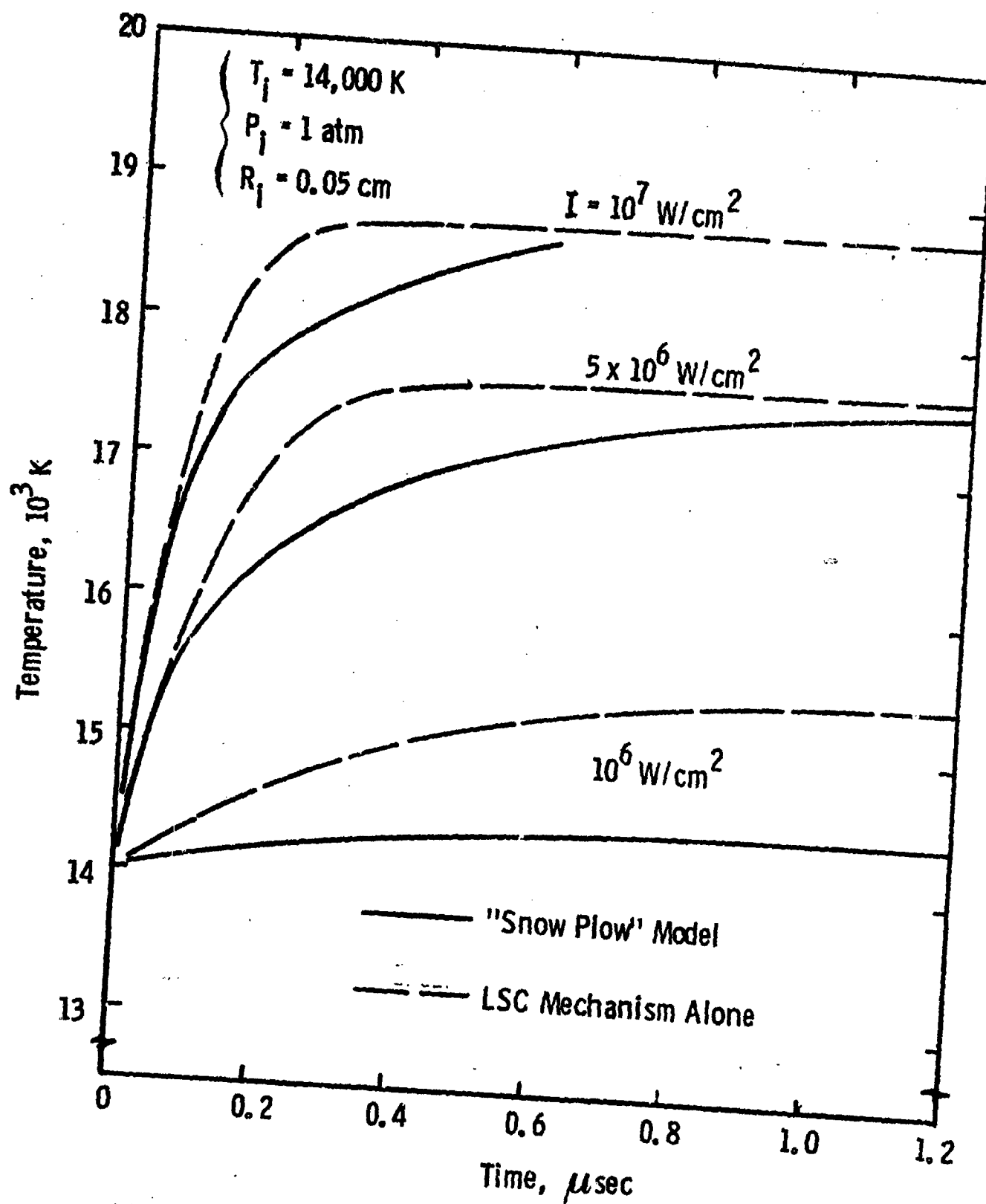


Fig. 5.4 The Temperature Distributions of Air Plasma for Various Laser Intensities.

where E_a is the laser absorption term which can readily be derived for uniform temperature to be

$$E_a = \frac{3I}{2\rho R} \left\{ \frac{1}{2} + \frac{1}{2RK_v} e^{-2RK_v} - \frac{1}{(2RK_v)^2} \left(1 - e^{-2RK_v} \right) \right\}$$

and the internal energy can be expressed as

$$e = h(T) - \frac{P}{\rho}$$

Finally, Eqs. (5.16) - (5.19) together with the equation of state

$$p = \rho \tilde{R} T \quad (5.20)$$

provide five equations for the five unknowns ρ , T , P , R and u_R . The enthalpy $h = h(T, P)$ is obtained from the results of Yos.⁴⁴ The above equations have been solved numerically for an initial temperature of 14,000 K, initial pressure of 1 atm and laser intensities of 10^6 , 5×10^6 and 10^7 W/cm². As shown in Fig. 5.4 for the case of $R_i = 0.05$ cm, the temperature distributions are not significantly different between the "snow plow" model and the calculations considering only the LSC mechanism, because the energy equation is dominated by the radiative transports. However, the air plasma growth rate has increased a great deal due to the hydrodynamic effects. For $R_i = 0.05$ cm and $I = 5 \times 10^6$ W/cm², the air plasma radius doubles in approximately 1 μ sec, (cf Fig. 5.5). One notes that the acceleration occurs in an early time and for each intensity the velocity reaches a different plateau. For all practical purposes, we can use the plateau velocity for each intensity to assess the air plasma growth rate in the pulse time of interest.

The plateau values of the expansion velocity are plotted against the laser intensity in Fig. 5.6. Since the particulates maybe only partially vaporized, calculations have also been done for $R_i = 0.025$, 0.010 and 0.005 cm. For

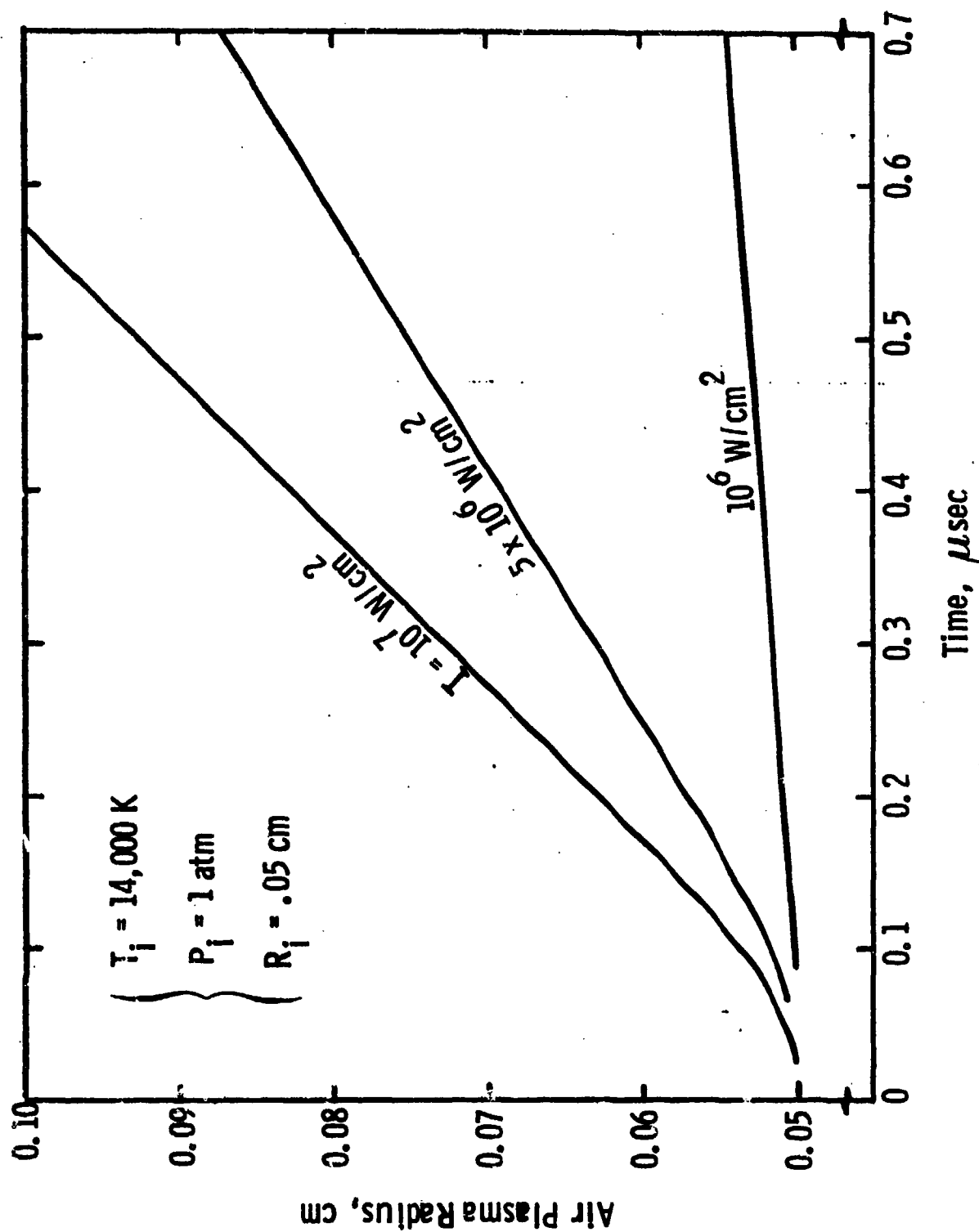


Fig. 5.5 The Air Plasma Growths as Function of Laser Intensity (Snow Plow Model).

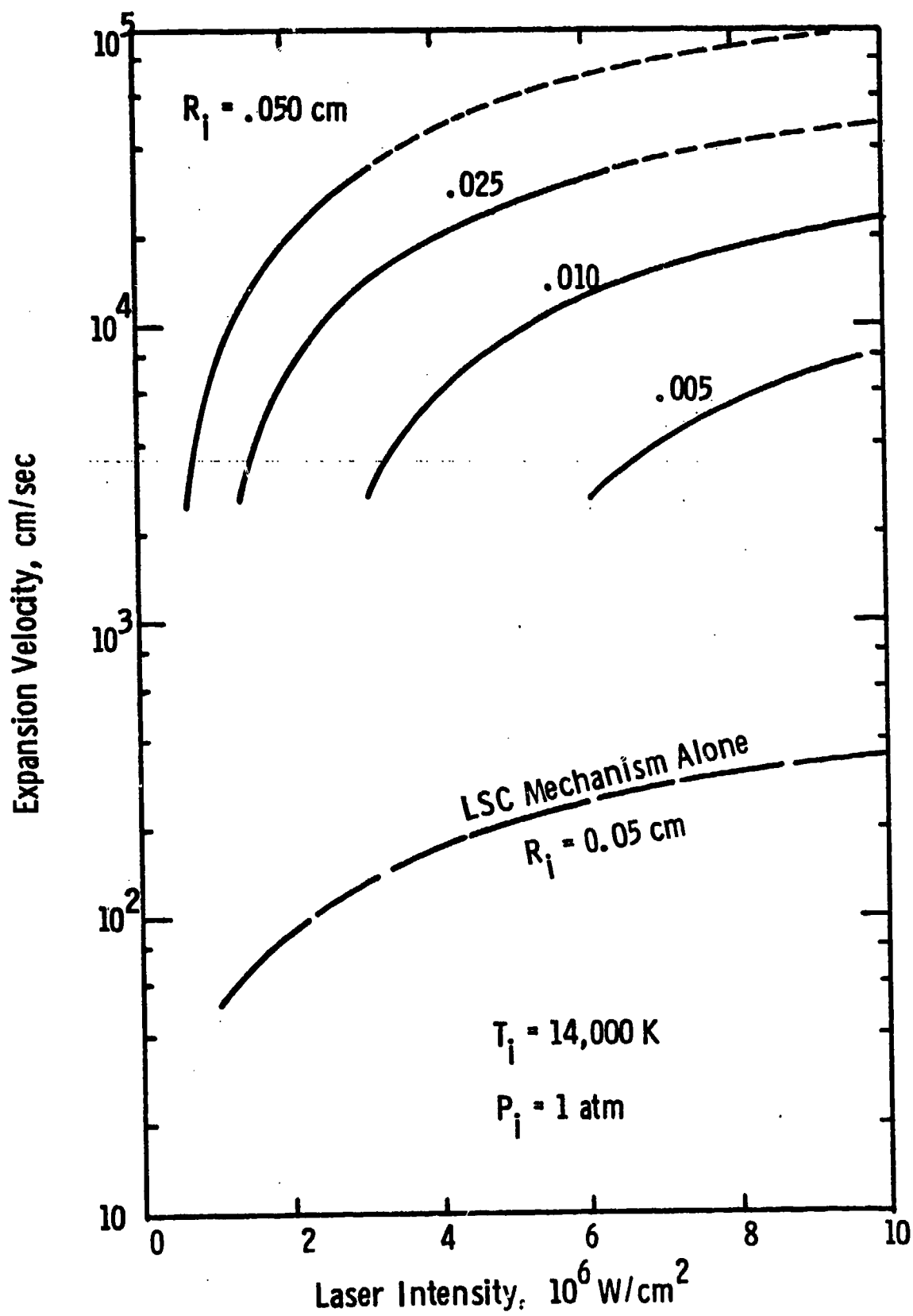


Fig. 5.6 Expansion Velocity of Air Plasma vs. Laser Intensity For Various Initial Radius.

comparison, the results for $R_i = 0.05$ cm from the perturbation calculations are also presented. It can be observed that although the LSC mechanism is vital in ingesting the high density ambient air, the air plasma growth is primarily a hydrodynamic effect, and that for a given pulse width a decrease in R_i requires an increase in laser intensity in order to reach a given final air plasma size. When the expansion velocity passes a value of about 3×10^4 cm/sec, which is the sound speed in the ambient air, the results imply that there will be shock wave proceeding the air plasma front. This phenomenon has not been accounted for in the present analysis. Consider an arbitrarily chosen final air plasma size to be 1 cm in diameter. Figure 5.7 shows the intensity requirement for a given initial size air plasma to grow to 1 cm in diameter in 50 and 100 μ sec. Suppose that we have a 20 cm diameter laser beam with an intensity of 4×10^6 W/cm² and the particulate distribution is such to provide an average initial air plasma bubble size of $R_i = .025$ cm. Then, when the number density of these bubbles is greater than 1.3 cm^{-2} across the beam, the air plasma will be able to fill-up the beam's cross section in 50 μ sec.

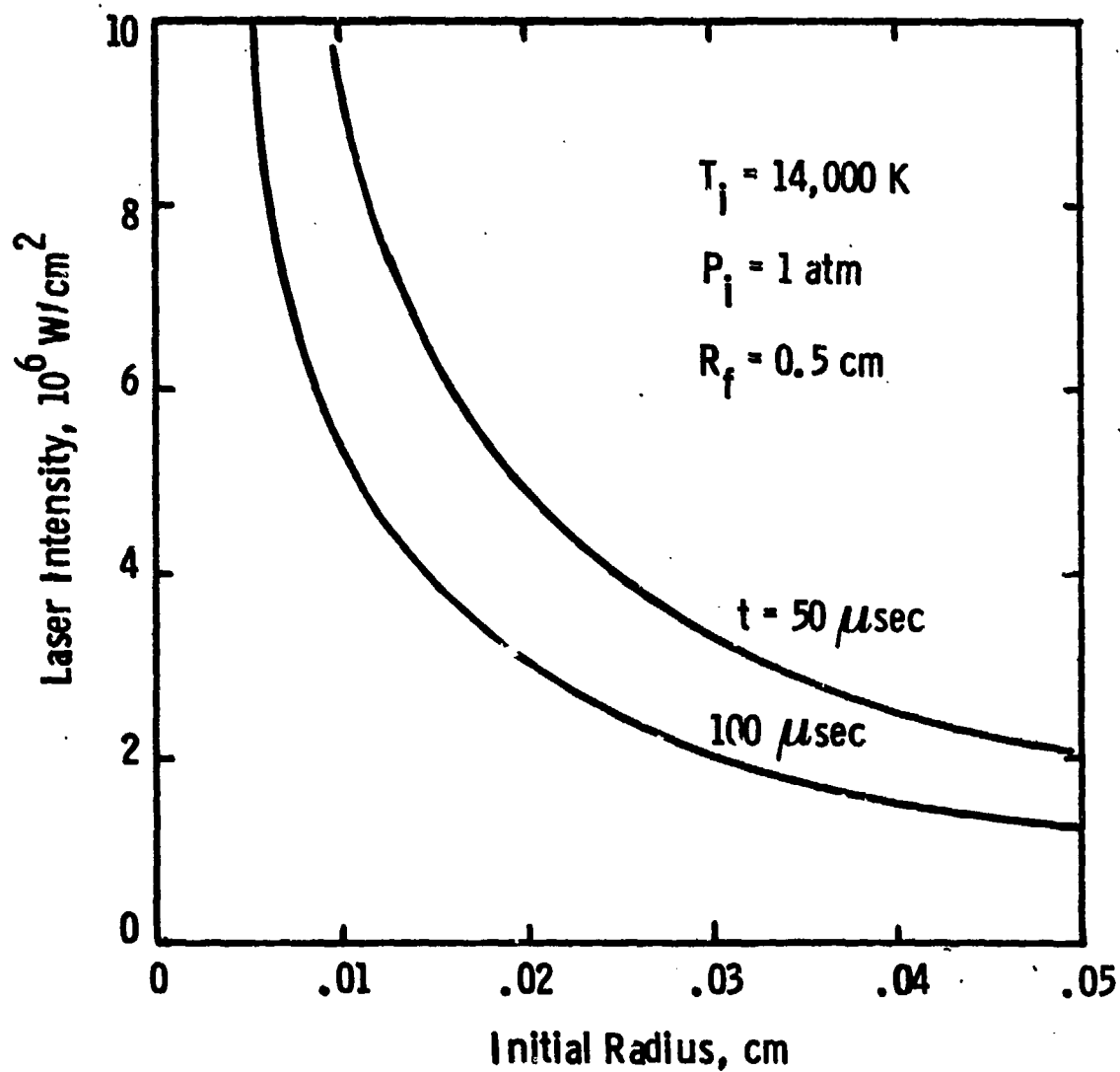


Fig. 5.7 The Required Laser Intensity for an Air Plasma to Reach 1 cm in Diameter in a Given Time (50 or 100 μsec) as Function of Initial Radius.

6. SUMMARY

The features of long pulse breakdown in particulate contaminated air which distinguish it from short pulse breakdown are: (1) low threshold intensities of the order of several megawatts per square centimeter, (2) long delay times of the order of tens of microseconds, and (3) the production of a luminous plasma several microseconds before breakdown occurs. These features suggest that breakdown occurs via heating of the particulate vapor at constant pressure and in thermodynamic equilibrium, with the subsequent production of an air plasma through energy transfer from the hot vapor. This mechanism is studied theoretically in the four preceding sections, and the results of the investigation are consistent with experimental observations.

As an example, consider an alumina particle having a diameter of 30μ . When this particle is subjected to $5 \times 10^6 \text{ W/cm}^2$ of 10.6μ radiation, we predict the following time scales: (1) The particle is 50% vaporized within 23 microseconds, (2) The luminous vapor thus formed heats without losses and reaches 20000°K within 14 microseconds, (3) The hot vapor cloud transfers energy to the surrounding air, thereby enabling the air to absorb laser radiation. The radius of the plasma is doubled within $2\mu\text{seconds}$. (4) The air plasma expands from a radius of .2 cm to a radius of .5 cm within 5 microseconds. (5) The total time from laser turn on to production of an air plasma one centimeter in diameter is therefore of the order of 44 microseconds, which is in agreement with the data of Ref. 4.

Even though the model is consistent with experiment, there remain several internal inconsistencies which should be eliminated if precise predictions are to be made. For example, the vapor production and vapor

6. SUMMARY

The features of long pulse breakdown in particulate contaminated air which distinguish it from short pulse breakdown are: (1) low threshold intensities of the order of several megawatts per square centimeter, (2) long delay times of the order of tens of microseconds, and (3) the production of a luminous plasma several microseconds before breakdown occurs. These features suggest that breakdown occurs via heating of the particulate vapor at constant pressure and in thermodynamic equilibrium, with the subsequent production of an air plasma through energy transfer from the hot vapor. This mechanism is studied theoretically in the four preceding sections, and the results of the investigation are consistent with experimental observations.

As an example, consider an alumina particle having a diameter of 30μ . When this particle is subjected to $5 \times 10^6 \text{ W/cm}^2$ of 10.6μ radiation, we predict the following time scales: (1) The particle is 50% vaporized within 23 microseconds, (2) The luminous vapor thus formed heats without losses and reaches 20000°K within 14 microseconds, (3) The hot vapor cloud transfers energy to the surrounding air, thereby enabling the air to absorb laser radiation. The radius of the plasma is doubled within $2\mu\text{seconds}$. (4) The air plasma expands from a radius of .2 cm to a radius of .5 cm within 5 microseconds. (5) The total time from laser turn on to production of an air plasma one centimeter in diameter is therefore of the order of 44 microseconds, which is in agreement with the data of Ref. 4.

Even though the model is consistent with experiment, there remain several internal inconsistencies which should be eliminated if precise predictions are to be made. For example, the vapor production and vapor

heating are clearly coupled since both processes operate over the same time scales. Similarly the final stage of vapor heating, the creation of an air plasma and the subsequent expansion of the air plasma all proceed at similar rates and should be united into one continuous process.

Further experimental data would be helpful for making refinements to the model. Experiments should be carried out with beams which are uniform over the size of the vapor cloud, say .2 cm. If the intensity does not remain constant throughout the pulse, the important quantity for breakdown calculations is the fluence at breakdown, not the time. Measurements made on a variety of different size alumina particles having radii greater than 30μ would aid in determining whether the observed threshold is caused by a requirement that the vapor be pure or a requirement that the cloud be a certain size. The threshold intensity should not change with increasing particle size if the threshold is related to the purity of the cloud. On the other hand, if the threshold is related to the size of the cloud, a larger particle will have a lower threshold. The composition of the luminous plasma can be investigated by observing atomic line spectra. The fluence at which the luminous vapor first appears reveals information about the particulate vaporization time. Finally, of course, comprehensive experiments should also be conducted with different particulates and at different wavelengths.

In conclusion, we have shown that the long pulse breakdown of air containing 30 micron alumina particles can be explained by a model based upon laser heating of the particulate vapor with the subsequent transfer of energy from the heated vapor plasma to the surrounding air. However the mechanism depends upon several details of the laser - particulate interaction which cannot be easily extrapolated to different wavelengths or to particulates having a different composition.

REFERENCES

1. D. E. Lencioni, Presentation at HELREG Subpanel Propagation Meeting, November 18, 1975, MITRE Corporation, Bedford, Mass.
2. D. E. Lencioni, "Laser-induced Air Breakdown for $1.06\text{ }\mu\text{m}$ Radiation", Applied Physics Letters, Vol. 25, No. 1, July 1, 1974, p. 15.
3. J. R. Triplett, and A. A. Boni, "The Interaction of Suspended Atmospheric Particles with Laser Radiation", Systems, Sciences and Software Rept. SSS-R-71-1167, June 1972.
4. R. E. Schlier, A. N. Pirri and D. J. Reilly, "Air Breakdown Studies", Air Force Weapons Lab., Rept. AFWL-TR-72-74, February 1973.
5. P. D. Thomas, "Laser Absorption Wave Formation", AIAA Journal, 13, 1279 (1975).
6. A. N. Pirri, "Analytic Solutions for Laser-Supported Combustion Wave Ignition above Surfaces", AIAA Paper No. 76-23, AIAA Aerospace Sciences Meeting, Washington, D. C., January 26, 1976.
7. H. C. Van de Hulst, Light Scattering by Small Particles, John Wiley and Sons, New York, 1957.

M. Born and E. Wolf, Principles of Optics, 3rd Ed. Pergamon Press, Oxford, 1965.
8. O. B. Toon and J. B. Pollack, J. Geophys. Res. 81, 5733 (1976).
9. G. Galand and H. Kirch, "Particulate Optical Properties in Rocket Plumes", AFRPL-TR-73-99, Lockheed Palo Alto Research Lab., Palo Alto, CA. (Nov. 1973).
10. M. E. Whitson, Jr., "Handbook of the Infrared Optical Properties of Al_2O_3 , Carbon, MgO , and ZrO_2 , Vol. I", SAMSO-TR-131, Vol. 1, The Aerospace Corp., El Segundo, CA. (June 1975).
11. J. V. Dave, "Subroutines for Computing the Parameters of the Electromagnetic Radiation Scattered by a Sphere", Rept. No. 320-3237, IBM Scientific Center, Palo Alto, CA. (May 1968).

REFERENCES (Cont'd)

12. Mie theory is capable of predicting deposition within a spherical particle. In the usual applications of Mie theory, however, attention is focussed on the scattering properties and overall absorption. Local deposition studies are seldom undertaken, and are not included in the code.
 13. In their study of absorption and heating of water droplets, G. E. Caledonia and J. D. Teare ("Aerosol Propagation Effects" PSI TR-13, Physical Sciences Inc, Woburn, MA (September 1974)) also resorted to ray optics in order to study the local energy deposition rate.
 14. This expression reduces to the equation derived by Caledonia and Teare (Ref. 13) when $n_1 \geq 1$.
 15. D. R. Stull and H. Prophet, Eds., "JANAF Thermochemical Tables", 2nd Edition, U. S. Dept. of Commerce NSRDS-NBS37, Washington, D. C.
 16. C. E. Moore, "Atomic Energy Levels", NSRDS-NBS-35, Vol. I, (Dec. 1971).
 17. D. E. Gray, Ed., American Institute of Physics Handbook, 2nd Ed., McGraw-Hill, New York (1963) p. 4-98.
 18. W. J. Karzas and R. Latter, Astrophys. Jour. Supplement 55, 6, 167 (1961).
 19. Ya. B. Zel'dovich and Yu. P. Raizer, Physics of Shock Waves and High Temperature Hydrodynamic Phenomena, Vol. I, Academic Press, New York, 1966, p. 259.
 20. H. A. Hyman and B. Kivel, J. Q. S. R. T. 13, 699 (1973).
 21. R. R. Teachout and R. T. Pack, Atomic Data 3, 195 (1971).
 22. R. L. Taylor and G. Caledonia, "Experimental Determination of the Cross Section for Neutral Bremsstrahlung II. High Temperature Air Species-O, N and N₂," SAMSO-TR-68-375, Avco-Everett Research Lab., Everett, MA (Feb. 1973).
- G. E. Caledonia, P.K.S. Wu and A. N. Pirri, "Radiant Energy Absorption Studies for Laser Propulsion", NASA CR-134809, Physical Sciences Inc., Woburn, MA (March 1975).

REFERENCES (Cont'd)

23. Private Communication.
24. R. A. McClatchey and J. E. A. Selby, "Atmospheric Attenuation of Laser Radiation from 0.76 to 31.25 μm " AFCRL-TR-74-0003 (Jan. 1974).
25. K. G. P. Sulzman, J. Q. S. R. T. 13, 931 (1973).
26. C. B. Ludwig, W. Malkmus, J. E. Reardon and J. A. L. Thomson, "Handbook of Infrared Radiation from Combustion Gases", NASA SP-3080.
27. S. S. Penner, Quantitative Molecular Spectroscopy and Gas Emissivities, Addison-Wesley Publishing Company, Inc., Reading, MA. (1959) p. 45.
28. H. H. Michels, "Diatomic Oxide Vibrational Band Intensities", K921094, United Aircraft Research Lab., East Hartford, Conn. (May 1971).
29. Experimentally measured f numbers for a band depend upon the temperature at which they are measured. Normally, however, the measurements are made at 300°K where only the lower rotational levels are occupied, so that the measured f number is close to the value for the lowest rotational state.
30. H. S. Carslaw and J. C. Jaeger, Conduction of Heat in Solids, Oxford University Press, London (1947) p. 209.
31. J. M. Yos, "Revised Transport Properties for High Temperature Air and its Components", (Nov. 1967).
32. R. C. Weast, Ed., Handbook of Chemistry and Physics, CRC Press Inc., (1975).
33. J. Crank, Mathematics of Diffusion, Oxford University Press, Oxford (1964) p. 29.
34. R. D. Hudson and L. J. Kieffer, "Compilation of Ultraviolet Photoabsorption Cross Sections for Atoms Between 5 and 3500 Å", NASA SP-3064 (1971).

REFERENCES (Cont'd)

35. G. M. Thomas and T. M. Helliwell, J.Q.S.R.T. 10, 423 (1970).
36. See, for example, p. 265 of Ref. 19 with the effective quantum number defined by

$$n_{\text{eff}} = \left(\frac{E_H}{E_{\infty} - E_n} \right)^{1/2}$$

where E_H is the ionization potential of hydrogen, E_{∞} is the ionization potential of atom and E_n is the energy of the n^{th} state.

37. W. L. Wiese, M. W. Smith and B. M. Miles, "Atomic Transition Probabilities Sodium through Calcium" NSRDS-NBS 22, Vol. II (October 1969).
38. W. L. Wiese, M. W. Smith and B. M. Glennon "Atomic Transition Probabilities Hydrogen through Neon" NSRDS-NBS 4, Vol. I (May 1966).
39. H. R. Griem, Plasma Spectroscopy, McGraw-Hill, New York, (1964).

H. R. Griem, Spectral Line Broadening by Plasmas, Academic Press, New York, (1974).
40. W. J. Hooker and R. P. Main "AIO (A-X) Oscillator Strengths and Collision Excitation Rates" ARPA Order No. 1482, KMS Technology Center, San Diego CA (March 1971).
41. Yu. P. Razier, JETP 31, 1148 (1970).
42. F. Y. Su and A. A. Boni, "Nonlinear Model of Laser Supported Deflagration Waves", Phys. Fluids 19, 960 (1976).

A. A. Boni and F. Y. Su, "Subsonic Propagation of Laser Supported Waves", AIAA paper 74-567.

A. A. Boni, H. D. Cohen, D. A. Miskan and F. Y. Su, "Laser-Interaction Studies", SSS-R-74-2344 (Aug. 1974).

J. P. Jackson and P. E. Nielsen, AIAA 12, 1498 (1974).

REFERENCES (Cont'd)

43. A. N. Pirri, N. H. Kemp, R. G. Root and P.K.S. Wu, "Theoretical Laser Effects Study", Final Rpt., PSI TR89, Feb. 1977.
44. J. M. Yos, "Transport Properties of Nitrogen, Hydrogen, Oxygen and Air to 30,000°K", Avco Corporation, Technical Memorandum, RAD-TM-63-7, March 1963.